

# **$WH$ production at the LHC within SMEFT at next-to-next-to-leading order QCD**

Marco Bonetti<sup>1,2,3,\*</sup>, Robert V. Harlander<sup>3,†</sup>, Dmitrii Korneev<sup>3,‡</sup>, Ming-Ming Long<sup>4,§</sup>, Kirill Melnikov<sup>4,||</sup>,  
Raoul Röntsch<sup>5,6,¶</sup> and Davide Maria Tagliabue<sup>4,5,6,\*\*</sup>

<sup>1</sup>*Institute for Astroparticle Physics, KIT, D-76344 Eggenstein Leopoldshafen, Germany*

<sup>2</sup>*Institute for Theoretical Physics, KIT, D-76128 Karlsruhe, Germany*

<sup>3</sup>*Institute for Theoretical Particle Physics and Cosmology, RWTH Aachen University, Sommerfeldstrasse 16, D-52056 Aachen, Germany*

<sup>4</sup>*Institute for Theoretical Particle Physics, KIT, D-76128 Karlsruhe, Germany*

<sup>5</sup>*Tif Lab, Dipartimento di Fisica, Università di Milano, Milan, Italy*

<sup>6</sup>*INFN, Sezione di Milano, Via Celoria 16, I-20133 Milan, Italy*



(Received 6 March 2025; accepted 31 July 2025; published 27 August 2025)

We study the impact of the pointlike  $q\bar{q}'WH$  interactions originating from a subset of dimension-six operators of the Standard Model effective field theory (SMEFT) on the Higgs boson associated production  $pp \rightarrow W^+H$  at the LHC. For consistency, we also take into account the corresponding  $q\bar{q}'W$  vertices implied by these operators. We compute the next-to-next-to-leading order quantum chromodynamics (QCD) corrections to this process and compare these corrections in the Standard Model and SMEFT production mechanisms.

DOI: [10.1103/ct5x-hl46](https://doi.org/10.1103/ct5x-hl46)

## **I. INTRODUCTION**

Despite its enormous success in describing elementary particles and their interactions, the Standard Model (SM) of particle physics leaves many questions related to its structure unanswered, and some key phenomenological observations unexplained [1]. A theory that addresses the structural shortcomings of the SM will likely be characterized by an energy scale which is so large that the direct production of new particles, related to such a theory, will not be possible at the Large Hadron Collider (LHC), and perhaps even at future particle colliders. For this reason, searches for physics beyond the SM are currently focused on *high-precision* studies of various SM processes at the LHC and elsewhere, with the hope of uncovering off-shell effects of as-of-yet unconfirmed quantum fields.

The SM effective field theory (SMEFT), an effective field theory built from the SM fields and gauge symmetries, is a helpful theoretical tool to parametrize such effects in a largely model-independent way. Assuming that the new physics scale  $\Lambda$  is much larger than the electroweak scale, which is set by the Higgs vacuum expectation value  $v = 246$  GeV, the SMEFT Lagrangian describes effects from beyond the Standard Model (BSM) physics in terms of local operators with mass dimensions  $\kappa > 4$ . These operators appear in the Lagrangian divided by  $\Lambda^{\kappa-4}$  and multiplied with dimensionless Wilson coefficients which are assumed to be of order one. At energies below  $\Lambda$ , the SMEFT contributions organize themselves into a hierarchical structure, whose leading term is the SM Lagrangian. The first subleading term is of order  $\Lambda^{-1}$  and arises from a single class of dimension-five operators of the form  $L_i L_j H H + \text{H.c.}$ , where  $L_i$  denotes the  $i$ th-generation lepton doublet, and  $H$  is the Higgs doublet [2]. These dimension-five operators may play an important role in various aspects of lepton and quark flavor physics but they are not important for hadron collider phenomenology.

At mass dimension six, the number of operators amounts to 3045 [3–6].<sup>1</sup> Their structure is quite diverse, ranging from a simple rescaling of SM parameters to operators that, if present, would lead to radically new phenomena such as lepton- and baryon-number violation. However, at such low

\*Contact author: marco.bonetti@kit.edu

†Contact author: harlander@physik.rwth-aachen.de

‡Contact author: kdmitry.de@gmail.com

§Contact author: ming-ming.long@kit.edu

||Contact author: kirill.melnikov@kit.edu

¶Contact author: raoul.rontsch@unimi.it

\*\*Contact author: davide.tagliabue@kit.edu

Published by the American Physical Society under the terms of the [Creative Commons Attribution 4.0 International](https://creativecommons.org/licenses/by/4.0/) license. Further distribution of this work must maintain attribution to the author(s) and the published article's title, journal citation, and DOI. Funded by SCOAP<sup>3</sup>.

<sup>1</sup>For completeness, let us point out that the full set of operators is known through mass dimension 12 [7].

orders in the SMEFT expansion, the set of operators relevant for a specific process is typically just a relatively small subset of the full operator basis. This allows us to focus on individual SM production processes and evaluate the impact of the SMEFT operators on them.

The Higgs sector is a particularly promising avenue to search for new physics since, on the one hand, it is still comparatively poorly explored and, on the other hand, its particular form in the SM is largely motivated by minimalistic considerations. A nonminimal character of this sector would imply nonvanishing Wilson coefficients in the SMEFT and could eventually manifest itself in the experimental data.

In this paper, we consider the process of associated Higgs production with a charged electroweak gauge boson,  $pp \rightarrow WH$ , at the LHC. Together with the related process  $pp \rightarrow ZH$ , it can be used to study the structure of the Higgs boson coupling to electroweak gauge bosons as well as the  $b$ -quark Yukawa coupling by means of jet-substructure techniques [8]. Furthermore, the similarity of  $ZH$  and  $WH$  production provides additional opportunities to search for new physics effects by studying peculiar differences between the two processes [9].

The SM predictions for  $VH$  production ( $V \in \{W, Z\}$ ) are under very good control. The fully differential cross sections are available through NNLO QCD [10–13], including the decay of the Higgs boson into bottom quarks [14–16], and through NLO in the electroweak coupling [17–19]. For the total inclusive cross section even the  $N^3$ LO QCD corrections are known [20].

The effect of all dimension-six operators from SMEFT which are relevant for  $VH$  production has been studied through NLO QCD in Ref. [21]. At NNLO QCD, the effects of higher-dimensional operators that lead to anomalous gauge-Higgs couplings were considered in Ref. [22]. Reference [23] evaluated QCD-induced SMEFT effects in  $ZH$  production, focussing on their impact on the subsequent decay of the Higgs boson into a  $b\bar{b}$  pair, and the SMEFT-induced rescaling of the SM couplings.

However, some operators that contribute to  $VH$  production induce interactions that are qualitatively different from the SM ones. Indeed, as we will show in the next section, some operators lead to four-point vertices that involve two quarks, a Higgs boson and a vector boson. The kinematical structure implied by such interactions may allow one to disentangle new physics effects from the typically dominant SM contributions. In particular, since the contributions of SMEFT operators increase at higher invariant masses and final-state transverse momenta [24], these phase-space regions constitute high-priority targets when searching for indirect new physics effects.

One may distinguish  $CP$ -even and  $CP$ -odd dimension-six operators relevant for  $VH$  production. The effect of the former type has been investigated, including NNLO QCD corrections and the matching to a parton shower, for both  $WH$  and  $ZH$  production [25]. In this paper, on the other hand, we also take into account the  $CP$ -odd operators,

focusing on  $W^+H$  production, and including the NNLO QCD corrections at the partonic level.

The remainder of the paper is organized as follows. In the next section, we provide the relevant information about the partonic contribution to the process  $pp \rightarrow W^+H$  in SMEFT including higher-dimensional operators and their impact. In Sec. III we report the calculation of all scattering amplitudes required for computing the NNLO QCD corrections in the presence of a nonstandard SMEFT interaction. In Sec. IV we perform phenomenological studies discussing the interplay of higher-order QCD corrections and higher-dimensional SMEFT operators in  $W^+H$  production at the LHC. We conclude in Sec. V. Additional information can be found in the Appendix and the Supplemental Material [26] provided with this submission.

## II. PROCESS DESCRIPTION

We consider the associated production of a  $W^+$  boson with a Higgs boson in the collision of a quark-antiquark pair, followed by the decay of the  $W^+$  boson into an electron-neutrino and a positron,

$$u(p_1)\bar{d}(p_2) \rightarrow W^+(\rightarrow \nu_e(p_3) + e^+(p_4)) + H. \quad (1)$$

In the SM, this process occurs through an intermediate off-shell  $W$  boson that is produced in  $q\bar{q}$  collisions and then decays into a Higgs boson and an on-shell  $W$  boson of momentum  $p_W = p_3 + p_4$ . We do not consider decays of the Higgs boson in this paper. The inclusion of dimension-six SMEFT operators leads to pointlike interactions between the quark pair and the Higgs and the  $W$  bosons, cf. Fig. 1(b). This local interaction is induced by the following SMEFT operators [27]:

$$\begin{aligned} Q_{\phi q}^{(3)} &= i(\phi^\dagger \overleftrightarrow{D}_\mu \phi)(\bar{q}_L \tau_I \gamma^\mu q_L), & Q_{\phi ud} &= i(\tilde{\phi}^\dagger D_\mu \phi)(\bar{u}_R \gamma^\mu d_R), \\ Q_{uW} &= (\bar{q}_L \sigma^{\mu\nu} u_R) \tau_I \tilde{\phi} W_{\mu\nu}^I, & Q_{dW} &= (\bar{q}_L \sigma^{\mu\nu} d_R) \tau_I \phi W_{\mu\nu}^I, \end{aligned} \quad (2)$$

where  $q_L = (u_L, d_L)$  denotes a left-handed quark doublet, and  $u_R$  and  $d_R$  are right-handed singlets. Here and in the

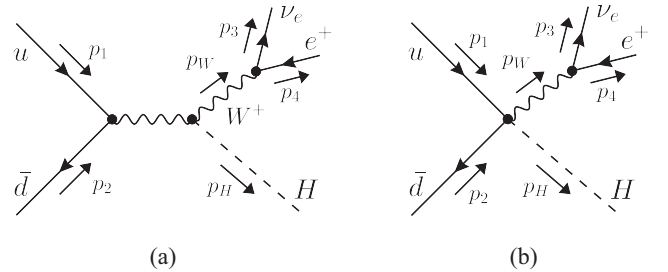


FIG. 1. Examples of diagrams that contribute to  $WH$  production at the LHC. (a) Contains both SM and SMEFT contributions, while (b) is present only in SMEFT.

following, by  $u$  and  $d$  we denote the up- and down-type quarks, respectively. The Higgs doublet is denoted by  $\phi$ , its dual by  $\tilde{\phi} = i\tau_2\phi^*$ ,  $W_{\mu\nu}^I$  is the field-strength tensor of the  $SU(2)_L$  gauge group,  $\tau^I$  are the Pauli matrices,  $\sigma^{\mu\nu} = i[\gamma^\mu, \gamma^\nu]/2$ , and

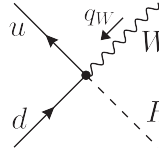
$$(\phi^\dagger \overleftrightarrow{D}_\mu \phi) = \phi^\dagger \tau^I (D_\mu \phi) - (D_\mu \phi^\dagger) \tau^I \phi. \quad (3)$$

The addition to the SM Lagrangian relevant for this paper reads

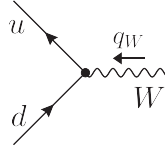
$$\delta\mathcal{L} = \frac{C_{\phi q}^{(3)}}{\Lambda^2} \mathcal{Q}_{\phi q}^{(3)} + \frac{C_{\phi ud}}{\Lambda^2} \mathcal{Q}_{\phi ud} + \frac{C_{uW}}{\Lambda^2} \mathcal{Q}_{uW} + \frac{C_{dW}}{\Lambda^2} \mathcal{Q}_{dW}. \quad (4)$$

The four quantities  $C_{\phi q}^{(3)}, C_{\phi ud}, C_{uW}, C_{dW}$  are the Wilson coefficients. There is an active program aiming at constraints on the SMEFT Wilson coefficients from fits to existing precision data. Assuming  $\Lambda = 1$  TeV, recent bounds on the first two coefficients give  $|C_{\phi q}^{(3)}| \lesssim 0.2$  and  $|C_{\phi ud}| \lesssim 0.13$  [28,29]. The imaginary parts of the latter two operators contribute to the neutron electric dipole moment and are thus tightly constrained [30]. Our results also depend on their real parts though, whose magnitude is restricted to about 0.3–0.5 (again assuming  $\Lambda = 1$  TeV) [31].

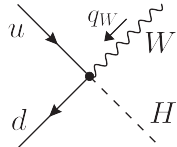
The Feynman rules relevant for our calculation induced by the operators of Eq. (2) are given by



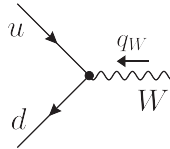
$$= C_1 \gamma_\mu \mathbb{P}_L + C_2 \gamma_\mu \mathbb{P}_R + C_3 \sigma_{\mu\nu} q_W^\nu \mathbb{P}_L + C_4 \sigma_{\mu\nu} q_W^\nu \mathbb{P}_R, \quad (5)$$



$$= \left(S_1 + \frac{v}{2} C_1\right) \gamma_\mu \mathbb{P}_L + \frac{v}{2} C_2 \gamma_\mu \mathbb{P}_R + v C_3 \sigma_{\mu\nu} q_W^\nu \mathbb{P}_L + v C_4 \sigma_{\mu\nu} q_W^\nu \mathbb{P}_R, \quad (6)$$



$$= -C_1^* \gamma_\mu \mathbb{P}_L - C_2^* \gamma_\mu \mathbb{P}_R + C_3^* \sigma_{\mu\nu} q_W^\nu \mathbb{P}_R + C_4^* \sigma_{\mu\nu} q_W^\nu \mathbb{P}_L, \quad (7)$$



$$= \left(S_1 - \frac{v}{2} C_1^*\right) \gamma_\mu \mathbb{P}_L - \frac{v}{2} C_2^* \gamma_\mu \mathbb{P}_R + v C_3^* \sigma_{\mu\nu} q_W^\nu \mathbb{P}_R + v C_4^* \sigma_{\mu\nu} q_W^\nu \mathbb{P}_L, \quad (8)$$

where  $q_W$  is the incoming momentum of the  $W$  boson,  $\mathbb{P}_{L,R} = (1 \pm \gamma_5)/2$  are the projection operators onto left- and right-handed helicity states,  $S_1 = -ig/\sqrt{2}$  is the SM  $Wq\bar{q}'$  coupling, and  $v$  is the Higgs field vacuum expectation value in the SM. The four constants  $C_{1,2,3,4}$  are related to the Wilson coefficients of the four operators, cf., Eq. (4). They read

$$\begin{aligned} C_1 &= -i\sqrt{2}gv \frac{C_{\phi q}^{(3)}}{\Lambda^2}, & C_2 &= -\frac{igv}{\sqrt{2}} \frac{C_{\phi ud}}{\Lambda^2}, \\ C_3 &= -2 \frac{(C_{uW})^*}{\Lambda^2}, & C_4 &= -2 \frac{C_{dW}}{\Lambda^2}. \end{aligned} \quad (9)$$

Furthermore, we use  $g = 2m_W/v = e/\sin\theta_W$ , where  $m_W$  is the mass of the  $W$  boson,  $e > 0$  is the positron charge and

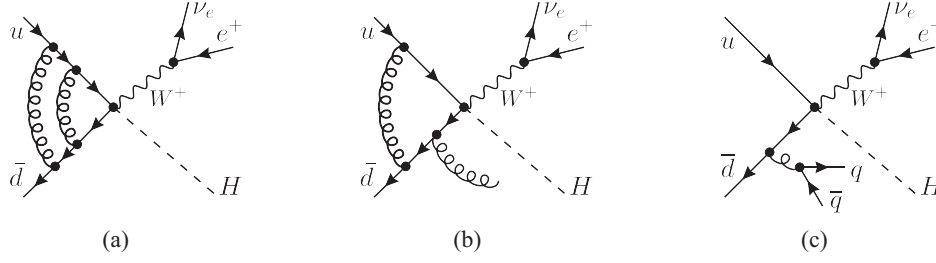


FIG. 2. Representative NNLO contributions to  $pp \rightarrow W^+H$ , for double-virtual corrections (a), real-virtual corrections (b), and double-real corrections (c).

$\theta_W$  is the weak mixing angle.<sup>2</sup> The operators  $Q_{uW}$  and  $Q_{dW}$  also induce interactions with two gauge bosons which contribute at higher orders in the electroweak coupling and are thus irrelevant within the scope of this paper. The same comment applies to Feynman rules involving two Higgs bosons arising from  $Q_{\phi q}^{(3)}$  and  $Q_{\phi ud}$ .

In principle, the Wilson coefficients in Eq. (9) depend on the quark generation. For simplicity, we will neglect this dependence. Furthermore, for our purpose of investigating the effects of non-SM interactions and their interplay with QCD corrections, we also replace the CKM matrix with the identity.<sup>3</sup> Finally, we do not consider possible SMEFT corrections to the decay of the  $W$  boson into a positron and an electron-neutrino.

### III. CALCULATION OF THE AMPLITUDES

To compute NNLO QCD corrections to the process in Eq. (1), we need to account for double-virtual, real-virtual and double-real contributions. Hence, we require the scattering amplitudes for the following processes:

- (i)  $0 \rightarrow \bar{u}d\nu_e e^+ H$  through two loops;
- (ii)  $0 \rightarrow \bar{u}d\nu_e e^+ H + g$  through one loop;
- (iii)  $0 \rightarrow \bar{u}d\nu_e e^+ H + gg$  and  $0 \rightarrow \bar{u}d\nu_e e^+ H + q\bar{q}$  at tree-level,

where  $q$  is any of the five quarks (up, down, charm, strange, bottom) that can be considered massless. Representative diagrams for each of these three contributions are shown in Fig. 2 for the pointlike  $q\bar{q}'WH$  interactions.

For completeness, let us remark that there are contributions involving a closed top-quark loop from which the Higgs boson is radiated, see, e.g., Fig. 3(a). In the SM, such terms were first considered in Ref. [32]. They are proportional to the second power of the strong coupling constant  $\alpha_s$ , and are finite and gauge invariant. They are sensitive to BSM modifications of the top Yukawa coupling, which is not the topic of our current paper. We therefore defer the study of

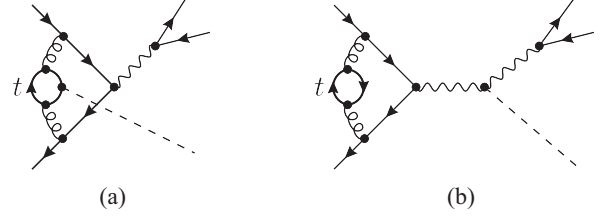


FIG. 3. Contributions involving top quark loops, where the Higgs may be radiated from the top loop (a) or from the  $W$  boson (b). They are neglected in this paper for reasons discussed in the main text.

these terms to future work. Other contributions involving closed top-quark loops factorize into Drell-Yan-like  $W$  production and subsequent decay into  $WH$ , see Fig. 3(b), for example. In the SM, they are suppressed by two to three orders of magnitude with respect to the remaining NNLO contributions [32–34]. We also expect a similar degree of suppression if the amplitude is mediated by the SMEFT operators, and neglect such contributions in our calculation.

Since we consider the production of the  $W$  boson in the narrow width approximation, any amplitude we need to compute can be written as a product of hadronic and leptonic currents, divided by the mass and the width of the  $W$  boson,

$$\mathcal{A} = -\frac{\mathcal{H}_\mu \mathcal{L}^\mu}{\Gamma_W m_W}. \quad (10)$$

The denominator arises from the on-shell ( $p_W^2 \rightarrow m_W^2$ ) limit of the  $W$  boson propagator<sup>4</sup>

$$\lim_{p_W^2 \rightarrow m_W^2} \frac{-ig^{\mu\nu}}{p_W^2 - m_W^2 + i\Gamma_W m_W} = \frac{-g^{\mu\nu}}{\Gamma_W m_W}. \quad (11)$$

The leptonic current is always left-handed; in the spinor-helicity formalism (for a review, see Ref. [35]), we can write it as

$$\mathcal{L}^\mu(p_3, p_4) = \langle 3 | \gamma^\mu | 4 \rangle. \quad (12)$$

<sup>2</sup>All the parameters listed here are SM-like, thanks to the fact that we do not consider SMEFT corrections involving  $Q_{\phi WB}$  or  $Q_{\phi D}$  operators, see Ref. [27].

<sup>3</sup>For the SM  $WH$  associated production, this approximation is accurate to about one percent.

<sup>4</sup>There is no technical obstacle to including off-shell effects, but we neglect them as they are suppressed by  $\Gamma_W/m_W \sim 10^{-2}$ .



The effective vertices shown in Eqs. (5) to (8) contain terms either with one Dirac matrix  $\gamma^\mu$  or with  $\sigma^{\mu\nu}$ . It is therefore convenient to split the hadronic current accordingly. We write

$$\mathcal{H}^\mu = \mathcal{H}_1^\mu + \mathcal{H}_2^\mu, \quad (13)$$

where  $\mathcal{H}_1^\mu$  corresponds to terms containing  $\gamma^\mu$  and  $\mathcal{H}_2^\mu$  to the terms containing  $\sigma^{\mu\nu}$ . Similarly, we express the amplitude as a sum of two terms

$$\mathcal{A} = \mathcal{A}_1 + \mathcal{A}_2, \quad (14)$$

where

$$\mathcal{A}_i = -\frac{\mathcal{H}_{i,\mu}\mathcal{L}^\mu}{\Gamma_W m_W}, \quad i = 1, 2. \quad (15)$$

The two amplitudes  $\mathcal{A}_{1,2}$  can be computed separately. Furthermore, each of the amplitudes  $\mathcal{A}_{1,2}$  contains left- and right-handed projectors. These projectors select specific helicities of external quarks; for this reason, we discard these projections when computing helicity amplitudes and account for them later by choosing appropriate helicities of the quarks that contribute to matrix elements of particular operators. Furthermore, since the  $\gamma^\mu$  vertex conserves helicity, while the  $\sigma^{\mu\nu}$  vertex flips it, the two amplitudes  $\mathcal{A}_1$  and  $\mathcal{A}_2$  do not interfere and can be studied independently of each other. This implies that the  $\sigma^{\mu\nu}$  part of the amplitude does not interfere with the SM amplitude and that its contribution to the  $WH$  production cross section is suppressed by  $1/\Lambda^4$ , in spite of the fact that it originates from a dimension-six operator. We will comment on this further in the following section.

We employ standard techniques for higher-order calculations to compute the amplitudes  $\mathcal{A}_{1,2}$ . To this end, we generate Feynman diagrams using QGRAF [36] and process them using FORM [37] and *Mathematica* [38]. We describe particularities related to the calculation of one- and two-loop amplitudes below.

### A. Virtual corrections to $0 \rightarrow \bar{u}d\nu_e e^+ H$

In this section, we discuss the calculation of one- and two-loop virtual corrections to the process  $0 \rightarrow \bar{u}d\nu_e e^+ H$ . The vector ( $\gamma^\mu$ ) part of the hadronic amplitude is described by the familiar quark form factor (see Refs. [39,40] for the more recent results). We therefore write

$$\mathcal{H}_1^\mu = \mathcal{F}_{1,1}(s_{12})\bar{u}(p_2)\gamma^\mu v(p_1), \quad (16)$$

where  $u$  and  $v$  are Dirac spinors, and  $\mathcal{F}_{1,1}$  is the two-loop form factor which depends on  $s_{12} = (p_1 + p_2)^2$ . Throughout this section, we will use the convention that the four-momenta of all particles are outgoing; it is

straightforward to transform the results to physical kinematics by analytic continuation.

To the best of our knowledge, virtual corrections to amplitudes with the tensor ( $\sigma^{\mu\nu}$ ) currents are unknown. Thanks to the fact that such a current is helicity-flipping, the number of independent Lorentz structures that may appear is restricted. We specify the hadronic current  $\mathcal{H}_2$  for three- and four-point interaction vertices; as we will see, they are different because of the momentum flow in the tensor current.

For the four-point case, the most general form of the amplitude  $\mathcal{H}_2^\mu$  reads

$$\mathcal{H}_{2,4\text{pt}}^\mu = \mathcal{F}_1 \bar{u}(p_2)[\gamma^\mu, \not{p}_W]v(p_1) + \mathcal{F}_2 \bar{u}(p_2)v(p_1)p_1^\mu + \mathcal{F}_3 \bar{u}(p_2)v(p_1)p_2^\mu. \quad (17)$$

We note that in this case  $p_W = -p_H - p_1 - p_2$ . However, in the case of the three-point interactions,  $p_W$  is replaced by the momentum of the intermediate  $W$  boson  $p_{W^*} = -p_1 - p_2$  and the above expression simplifies. Hence, for the three-point interaction case, we write

$$\mathcal{H}_{2,3\text{pt}}^\mu = \mathcal{F}_4 \bar{u}(p_2)v(p_1)p_1^\mu + \mathcal{F}_5 \bar{u}(p_2)v(p_1)p_2^\mu. \quad (18)$$

Thanks to the structure of the interaction vertex that involves  $\sigma^{\mu\nu}p_{W,\nu}$ , the amplitude  $\mathcal{H}_2$  vanishes when contracted with the  $W$  boson momentum, resulting in

$$\begin{aligned} \mathcal{H}_{2,4\text{pt}} \cdot p_W &= 0, \\ \mathcal{H}_{2,3\text{pt}} \cdot p_{W^*} &= -\mathcal{H}_{2,3\text{pt}} \cdot (p_1 + p_2) = 0. \end{aligned} \quad (19)$$

We use Eq. (19) to rewrite  $\mathcal{H}_{2,4\text{pt}}$  in terms of two independent form factors

$$\mathcal{H}_{2,4\text{pt}}^\mu = \mathcal{F}_{2,1}T_1^\mu + \mathcal{F}_{2,2}T_2^\mu, \quad (20)$$

and  $\mathcal{H}_{2,3\text{pt}}$  in terms of a single form factor

$$\mathcal{H}_{2,3\text{pt}}^\mu = \mathcal{F}_{2,3}\bar{u}(p_2)v(p_1)(p_1^\mu - p_2^\mu). \quad (21)$$

In Eq. (20) we have used the following quantities

$$\begin{aligned} T_1^\mu &= \bar{u}(p_2)[\gamma^\mu, \not{p}_W]v(p_1), \\ T_2^\mu &= \bar{u}(p_2)v(p_1)(s_{2W}p_1^\mu - s_{1W}p_2^\mu), \end{aligned} \quad (22)$$

with  $s_{iW} = 2p_i \cdot p_W$ ,  $i = 1, 2$ , to write the amplitude.

The form factors can be extracted by applying the projection operators to the matrix element of the current  $\mathcal{H}_2^\mu$ . We do this separately for contributions that originate from three- and four-point interaction vertices. In the former case, projecting on  $\mathcal{F}_{2,3}$  is straightforward. In the latter case, we write

$$\mathcal{F}_{2,j} = \sum_{\text{pol}} \mathcal{P}_j \epsilon_W^* \cdot \mathcal{H}_{2,4\text{pt}}, \quad (23)$$

where  $\epsilon_W^*$  is the polarization vector of the  $W$  boson and we sum over polarizations of all external particles including quarks and the  $W$  boson. The projection operators  $\mathcal{P}_{j=1,2}$  can be written as linear combinations of the tensors  $\mathcal{T}_1^\dagger$  and  $\mathcal{T}_2^\dagger$

$$\mathcal{P}_j = \mathbf{R}_{jk} \mathcal{T}_{k,\mu}^\dagger \epsilon_W^\mu, \quad (24)$$

where the matrix  $\mathbf{R}$  reads

$$\mathbf{R} = \frac{1}{\mathcal{N}} \begin{pmatrix} s_{12}^2 s_{1W} s_{2W} & -2s_{12} s_{1W} s_{2W} \\ -2s_{12} s_{1W} s_{2W} & 4(d-2)s_{1W} s_{2W} - 4(d-3)s_{12} p_W^2 \end{pmatrix}. \quad (25)$$

The quantity  $\mathcal{N}$  is given by

$$\mathcal{N} = 8(3-d)s_{12}^2 s_{1W} s_{2W} (s_{12} p_W^2 - s_{1W} s_{2W}), \quad (26)$$

where  $d = 4 - 2\epsilon$  is the space-time dimension. The sum over  $W$  polarizations is given by the standard expression

$$\sum \epsilon_W^{\mu*} \epsilon_W^\nu = -g^{\mu\nu} + \frac{p_W^\mu p_W^\nu}{m_W^2}, \quad (27)$$

where the second term can be dropped because of Eq. (19).

Once the current  $\mathcal{H}_2^\mu$  is projected onto individual form factors, we make use of integration-by-parts identities [41,42] to reduce all one- and two-loop integrals to master integrals. For this purpose, we have used Reduze [43] and Kira [44–46] interfaced with FireFly [47,48]. The master integrals required to compute  $\mathcal{H}_1^\mu$  and  $\mathcal{H}_2^\mu$  are identical; they can be borrowed from Refs. [40,49]. Although, as mentioned earlier, we can take the vector form factor  $\mathcal{F}_{1,1}$  from the literature, we also recomputed it with the same setup we used to calculate the current  $\mathcal{H}_2^\mu$ , and found agreement with the known results in Ref. [40].

The calculation of the helicity amplitudes is straightforward. Starting from Eqs. (16)–(18), using Eq. (10), and fixing the helicities of external partons, we obtain

$$\begin{aligned} \mathcal{A}_1(p_1^+, p_2^-, p_3^-, p_4^+) &= \frac{2\mathcal{F}_{1,1}}{m_W \Gamma_W} \langle 23 \rangle [14], \\ \mathcal{A}_1(p_1^-, p_2^+, p_3^-, p_4^+) &= \frac{2\mathcal{F}_{1,1}}{m_W \Gamma_W} \langle 13 \rangle [24], \\ \mathcal{A}_2(p_1^-, p_2^-, p_3^-, p_4^+) &= -\frac{2\mathcal{F}_{2,1}}{m_W \Gamma_W} \langle 13 \rangle \langle 23 \rangle [34] - \frac{\langle 12 \rangle}{2m_W \Gamma_W} K, \\ \mathcal{A}_2(p_1^+, p_2^+, p_3^-, p_4^+) &= \frac{2\mathcal{F}_{2,1}}{m_W \Gamma_W} [14] [24] \langle 34 \rangle - \frac{[12]}{2m_W \Gamma_W} K, \end{aligned} \quad (28)$$

where  $K$  is given by

$$\begin{aligned} K &= \langle 13 \rangle [14] (s_{2W} \mathcal{F}_{2,2} + 2m_W^2 \Pi_{W^*} \mathcal{F}_{2,3}) \\ &\quad - \langle 23 \rangle [24] (s_{1W} \mathcal{F}_{2,2} + 2m_W^2 \Pi_{W^*} \mathcal{F}_{2,3}), \end{aligned} \quad (29)$$

with<sup>5</sup>

$$\Pi_{W^*} = \frac{1}{s_{12} - m_W^2 + im_W \Gamma_W}. \quad (30)$$

All other helicity amplitudes vanish thanks to the left-handed coupling between the  $W$  boson and the leptonic current.

Physical helicity amplitudes are constructed from the  $\mathcal{A}_i$  by restoring the electroweak couplings

$$\begin{aligned} \mathcal{M}(p_1^+, p_2^-, p_3^-, p_4^+) &= \delta_{i_1 i_2} C_W \left[ C_1 (1 + m_W^2 \Pi_{W^*}) \right. \\ &\quad \left. + \frac{2m_W^2 \Pi_{W^*}}{v} S_1 \right] \mathcal{A}_1(p_1^+, p_2^-, p_3^-, p_4^+), \\ \mathcal{M}(p_1^-, p_2^+, p_3^-, p_4^+) &= \delta_{i_1 i_2} C_W C_2 (1 + m_W^2 \Pi_{W^*}) \\ &\quad \times \mathcal{A}_1(p_1^-, p_2^+, p_3^-, p_4^+), \\ \mathcal{M}(p_1^-, p_2^-, p_3^+, p_4^+) &= \delta_{i_1 i_2} C_W C_3 \mathcal{A}_2(p_1^-, p_2^-, p_3^+, p_4^+), \\ \mathcal{M}(p_1^+, p_2^+, p_3^-, p_4^+) &= \delta_{i_1 i_2} C_W C_4 \mathcal{A}_2(p_1^+, p_2^+, p_3^-, p_4^+), \end{aligned} \quad (31)$$

where  $C_W = -ie/(\sqrt{2} \sin \theta_W)$  is the strength of the  $W$  boson coupling to the  $e^+ \nu_e$  pair,  $S_1$  and  $C_i$  have been defined in Sec. II, and  $i_{1,2}$  are color indices of the antiquark and quark.

The form factors that we obtained contain both ultra-violet (UV) and infrared (IR) divergences, appearing as poles in the dimensional regularization parameter  $\epsilon$ . For the vector current form factor, only the strong coupling constant needs to be renormalized. The relation between bare ( $\alpha_{s,0}$ ) and renormalized ( $\alpha_s$ ) strong coupling constants reads (see, e.g., [50])

$$\alpha_{s,0} \mu_0^{2\epsilon} S_\epsilon = \alpha_s \mu^{2\epsilon} \left[ 1 - \frac{\beta_0}{\epsilon} \frac{\alpha_s}{2\pi} + \mathcal{O}(\alpha_s^2) \right], \quad (32)$$

where  $S_\epsilon = (4\pi)^\epsilon e^{-\epsilon \gamma_E}$ ,

$$\beta_0 = \frac{11}{6} C_A - \frac{2}{3} n_f T_R, \quad (33)$$

with  $C_A = 3$ ,  $T_R = 1/2$ , and  $n_f$  denoting the number of light quark flavors.

In contrast to the case of the vector current, the tensor current  $\sigma_{\mu\nu} p_W^\nu$  is not conserved and, therefore, requires UV

<sup>5</sup>We note that it is customary to include the width term  $im_W \Gamma_W$  in the propagator of the intermediate  $W$  boson, although it cannot go on the mass shell since  $s_{12} > (m_W + m_H)^2$ .

renormalization. We perform the renormalization in the  $\overline{\text{MS}}$ -scheme. The corresponding renormalization constant can be extracted from Ref. [21] and reads

$$Z_{\mathcal{H}_2} = 1 + \frac{C_F \alpha_s}{2\epsilon 2\pi} + \left(\frac{\alpha_s}{2\pi}\right)^2 C_F \left[ C_A \left( -\frac{11}{24\epsilon^2} + \frac{257}{144\epsilon} \right) + C_F \left( \frac{1}{8\epsilon^2} - \frac{19}{16\epsilon} \right) + n_f T_R \left( \frac{1}{6\epsilon^2} - \frac{13}{36\epsilon} \right) \right] + \mathcal{O}(\alpha_s^3), \quad (34)$$

with  $C_F = 4/3$ . Once the UV renormalization is performed, we find that the remaining infrared pole structure of all amplitudes computed in this paper agrees with Catani's universal formula [50]. Additional details can be found in the Appendix.

As a check, we also evaluated the one- and two-loop amplitudes using an approach which generalizes the Passarino-Veltman reduction [51]. At two-loops, we used a combination of the Passarino-Veltman tensorial reduction and integration-by-parts identities to express tensor integrals through master integrals. In this way, the decomposition of amplitudes into invariant form factors shown in Eqs. (16), (20), and (21) appears as a natural result of the calculation.

A further consistency check can be performed by realizing that the Feynman rules for the three-point and the four-point SMEFT vertices become identical in the (formal) soft-Higgs limit,  $p_H \rightarrow 0$  (up to the coupling constants). We have explicitly checked this limit of the computed amplitudes, finding agreement among the different expressions.

Finally, we have checked the Born and the renormalized one-loop amplitudes numerically for multiple phase-space points against OpenLoops [52], MadGraph [53], and GoSam [54,55], finding perfect agreement. Results for renormalized

helicity amplitudes computed in this paper can be found in the Supplemental Material [26] provided with this submission.

### B. One-loop amplitudes for $0 \rightarrow \bar{u}d\nu_e e^+ H + g$

The second ingredient required for the NNLO calculation is the one-loop amplitude for the process  $0 \rightarrow \bar{u}d\nu_e e^+ H + g(p_5)$ . Similar to the two-loop case, we need to consider two currents  $\mathcal{H}_1^\mu$  and  $\mathcal{H}_2^\mu$  and select the appropriate helicity configurations to discuss their left- and right-handed components. The amplitudes  $0 \rightarrow \bar{u}d\nu_e e^+ H + g$  for the vector current can be extracted from Ref. [39], whereas the matrix element of the current with  $\sigma^{\mu\nu} p_{W,\nu}$  is unknown.

As discussed in Ref. [39], the matrix element of the current  $\mathcal{H}_1^\mu$  can be decomposed into seven independent Lorentz structures. The calculation of the matrix element of  $\mathcal{H}_2^\mu$  can be performed following similar steps, but it is much more complicated. In fact, after imposing two sets of conditions

$$\begin{aligned} \mathcal{H}_{2,4\text{pt}}^\mu \Big|_{\epsilon_5^* \rightarrow p_5} &= 0, & \mathcal{H}_{2,4\text{pt}} \cdot p_W &= 0, \\ \mathcal{H}_{2,3\text{pt}}^\mu \Big|_{\epsilon_5^* \rightarrow p_5} &= 0, & \mathcal{H}_{2,3\text{pt}} \cdot (p_1 + p_2 + p_5) &= 0, \end{aligned} \quad (35)$$

where  $\epsilon_5$  is the polarization vector of the radiated gluon, the matrix element of  $\mathcal{H}_2^\mu$  can be written as a linear combination of tensor structures

$$\mathcal{H}_2^\mu = \sum_{i=1}^{i_{\max}} \mathcal{F}_{2,i}^{(g)} T_i^\mu, \quad (36)$$

where  $i_{\max} = 7(16)$  for the three-point (four-point) SMEFT vertex. For the three-point vertex, they read

$$\begin{aligned} T_1^\mu &= [(s_{12} + s_{15})p_5^\mu - (s_{15} + s_{25})p_1^\mu] \bar{u}(p_2) \not{\epsilon}_5 \not{\epsilon}_5^* v(p_1), \\ T_2^\mu &= [(s_{12} + s_{25})p_5^\mu - (s_{15} + s_{25})p_2^\mu] \bar{u}(p_2) \not{\epsilon}_5 \not{\epsilon}_5^* v(p_1), \\ T_3^\mu &= \frac{2(p_1 \cdot \epsilon_5^*) \bar{u}(p_2) \gamma^\mu \not{\epsilon}_5 v(p_1)}{s_{15}} + \frac{2p_5^\mu \bar{u}(p_2) \not{\epsilon}_5 \not{\epsilon}_5^* v(p_1)}{s_{15} + s_{25}} - \bar{u}(p_2) \gamma^\mu \not{\epsilon}_5^* v(p_1), \\ T_4^\mu &= \frac{(s_{12} + s_{15})(s_{25}(p_1 \cdot \epsilon_5^*) - s_{15}(p_2 \cdot \epsilon_5^*)) \bar{u}(p_2) \gamma^\mu \not{\epsilon}_5 v(p_1)}{2s_{15}} - p_1^\mu \bar{u}(p_2) v(p_1) (s_{25}(p_1 \cdot \epsilon_5^*) - s_{15}(p_2 \cdot \epsilon_5^*)), \\ T_5^\mu &= \frac{(s_{12} + s_{25})(s_{25}(p_1 \cdot \epsilon_5^*) - s_{15}(p_2 \cdot \epsilon_5^*)) \bar{u}(p_2) \gamma^\mu \not{\epsilon}_5 v(p_1)}{2s_{15}} - p_2^\mu \bar{u}(p_2) v(p_1) (s_{25}(p_1 \cdot \epsilon_5^*) - s_{15}(p_2 \cdot \epsilon_5^*)), \\ T_6^\mu &= \frac{(s_{15} + s_{25})(s_{15}(p_2 \cdot \epsilon_5^*) - s_{25}(p_1 \cdot \epsilon_5^*)) \bar{u}(p_2) \gamma^\mu \not{\epsilon}_5 v(p_1)}{2s_{15}} + p_5^\mu \bar{u}(p_2) v(p_1) (s_{25}(p_1 \cdot \epsilon_5^*) - s_{15}(p_2 \cdot \epsilon_5^*)), \\ T_7^\mu &= \frac{2(p_2 \cdot \epsilon_5^*) \bar{u}(p_2) \gamma^\mu \not{\epsilon}_5 v(p_1)}{s_{25}} + \frac{2p_5^\mu \bar{u}(p_2) \not{\epsilon}_5 \not{\epsilon}_5^* v(p_1)}{s_{15} + s_{25}} - \frac{4p_5^\mu \bar{u}(p_2) v(p_1) (p_2 \cdot \epsilon_5^*)}{s_{25}} + \bar{u}(p_2) \not{\epsilon}_5^* \gamma^\mu v(p_1), \end{aligned} \quad (37)$$

whereas for the four-point vertex we find

$$\begin{aligned}
T_1^\mu &= \bar{u}(p_2)[\gamma^\mu, \not{p}_W]\not{p}_5\epsilon_5^*v(p_1), \\
T_2^\mu &= \bar{u}(p_2)\epsilon_5^*\not{p}_5[\gamma^\mu, \not{p}_W]v(p_1), \\
T_3^\mu &= (s_{1W}p_5^\mu - s_{5W}p_1^\mu)\bar{u}(p_2)\not{p}_5\epsilon_5^*v(p_1), \\
T_4^\mu &= (s_{2W}p_5^\mu - s_{5W}p_2^\mu)\bar{u}(p_2)\not{p}_5\epsilon_5^*v(p_1), \\
T_5^\mu &= \bar{u}(p_2)[\gamma^\mu, \not{p}_W]v(p_1)[s_{25}(\epsilon_5^* \cdot p_1) - s_{15}(\epsilon_5^* \cdot p_2)], \\
T_6^\mu &= \left[ p_1^\mu \bar{u}(p_2)\not{p}_W\not{p}_5v(p_1) - \frac{1}{2}s_{1W}\bar{u}(p_2)\gamma^\mu\not{p}_5v(p_1) \right] [s_{25}(\epsilon_5^* \cdot p_1) - s_{15}(\epsilon_5^* \cdot p_2)], \\
T_7^\mu &= \left[ p_2^\mu \bar{u}(p_2)\not{p}_W\not{p}_5v(p_1) - \frac{1}{2}s_{2W}\bar{u}(p_2)\gamma^\mu\not{p}_5v(p_1) \right] [s_{25}(\epsilon_5^* \cdot p_1) - s_{15}(\epsilon_5^* \cdot p_2)], \\
T_8^\mu &= \left[ p_5^\mu \bar{u}(p_2)\not{p}_W\not{p}_5v(p_1) - \frac{1}{2}s_{5W}\bar{u}(p_2)\gamma^\mu\not{p}_5v(p_1) \right] [s_{25}(\epsilon_5^* \cdot p_1) - s_{15}(\epsilon_5^* \cdot p_2)], \\
T_9^\mu &= \frac{1}{2}s_{25}p_1^\mu\bar{u}(p_2)\not{p}_W\epsilon_5^*v(p_1) + \frac{1}{2}s_{1W}(\epsilon_5^* \cdot p_2)\bar{u}(p_2)\gamma^\mu\not{p}_5v(p_1) - p_1^\mu(\epsilon_5^* \cdot p_2)\bar{u}(p_2)\not{p}_W\not{p}_5v(p_1) - \frac{1}{4}s_{25}s_{1W}\bar{u}(p_2)\gamma^\mu\epsilon_5^*v(p_1), \\
T_{10}^\mu &= \frac{1}{2}s_{25}p_2^\mu\bar{u}(p_2)\not{p}_W\epsilon_5^*v(p_1) + \frac{1}{2}s_{2W}(\epsilon_5^* \cdot p_2)\bar{u}(p_2)\gamma^\mu\not{p}_5v(p_1) - p_2^\mu(\epsilon_5^* \cdot p_2)\bar{u}(p_2)\not{p}_W\not{p}_5v(p_1) - \frac{1}{4}s_{25}s_{2W}\bar{u}(p_2)\gamma^\mu\epsilon_5^*v(p_1), \\
T_{11}^\mu &= \frac{1}{2}s_{25}p_5^\mu\bar{u}(p_2)\not{p}_W\epsilon_5^*v(p_1) + \frac{1}{2}s_{5W}(\epsilon_5^* \cdot p_2)\bar{u}(p_2)\gamma^\mu\not{p}_5v(p_1) - p_5^\mu(\epsilon_5^* \cdot p_2)\bar{u}(p_2)\not{p}_W\not{p}_5v(p_1) - \frac{1}{4}s_{25}s_{5W}\bar{u}(p_2)\gamma^\mu\epsilon_5^*v(p_1), \\
T_{12}^\mu &= p_5^\mu\bar{u}(p_2)v(p_1)(\epsilon_5^* \cdot p_W) - \frac{1}{4}s_{5W}\bar{u}(p_2)\gamma^\mu\epsilon_5^*v(p_1) - \frac{1}{4}s_{5W}\bar{u}(p_2)\epsilon_5^*\gamma^\mu v(p_1), \\
T_{13}^\mu &= \bar{u}(p_2)v(p_1)(p_1^\mu(s_{15}(\epsilon_5^* \cdot p_W) - s_{5W}(\epsilon_5^* \cdot p_1)) + s_{1W}p_5^\mu(\epsilon_5^* \cdot p_1)) - \frac{1}{4}s_{15}s_{1W}\bar{u}(p_2)\gamma^\mu\epsilon_5^*v(p_1) - \frac{1}{4}s_{15}s_{1W}\bar{u}(p_2)\epsilon_5^*\gamma^\mu v(p_1), \\
T_{14}^\mu &= \bar{u}(p_2)v(p_1)(p_2^\mu(s_{15}(\epsilon_5^* \cdot p_W) - s_{5W}(\epsilon_5^* \cdot p_1)) + s_{2W}p_5^\mu(\epsilon_5^* \cdot p_1)) - \frac{1}{4}s_{15}s_{2W}\bar{u}(p_2)\gamma^\mu\epsilon_5^*v(p_1) - \frac{1}{4}s_{15}s_{2W}\bar{u}(p_2)\epsilon_5^*\gamma^\mu v(p_1), \\
T_{15}^\mu &= \bar{u}(p_2)v(p_1)(p_1^\mu(s_{25}(\epsilon_5^* \cdot p_W) - s_{5W}(\epsilon_5^* \cdot p_2)) + s_{1W}p_5^\mu(\epsilon_5^* \cdot p_2)) - \frac{1}{4}s_{25}s_{1W}\bar{u}(p_2)\gamma^\mu\epsilon_5^*v(p_1) - \frac{1}{4}s_{25}s_{1W}\bar{u}(p_2)\epsilon_5^*\gamma^\mu v(p_1), \\
T_{16}^\mu &= \bar{u}(p_2)v(p_1)(p_2^\mu(s_{25}(\epsilon_5^* \cdot p_W) - s_{5W}(\epsilon_5^* \cdot p_2)) + s_{2W}p_5^\mu(\epsilon_5^* \cdot p_2)) - \frac{1}{4}s_{25}s_{2W}\bar{u}(p_2)\gamma^\mu\epsilon_5^*v(p_1) - \frac{1}{4}s_{25}s_{2W}\bar{u}(p_2)\epsilon_5^*\gamma^\mu v(p_1).
\end{aligned} \tag{38}$$

In the above, we have defined  $s_{ij} = 2p_i \cdot p_j$ . We note that the reference vector for the gluon polarization has not been fixed in the above expressions.

We construct projection operators using the tensors in Eqs. (37), (38) to compute the form factors  $\mathcal{F}_{2,i}^{(g)}$ . Explicit expressions for the projection operators can be found in the Supplemental Material [26] provided with this submission.<sup>6</sup> Once the amplitudes are projected onto the individual form factors, we use integration-by-parts identities to reduce them to master integrals. We employ the analytic expressions for master integrals computed in Refs. [39,57,58]. Infrared divergencies in the amplitudes are described by Catani's

<sup>6</sup>We note that their construction requires the inversion of a very complicated and dense matrix, which turns out to be computationally expensive using standard *Mathematica* routines such as *Inverse*. We rely instead on the *FFInverse* function provided by the package *FiniteFlow* [56].

formula [50] which also serves as a useful check of the calculation.

Finally, we note that we computed the bare amplitudes using the Passarino-Veltman reduction as a cross-check, finding agreement with the result obtained using projection operators. We also compared the final result for the amplitude with OpenLoops [52], MadGraph [53], and GoSam [54,55] and found perfect agreement. The renormalized helicity amplitudes for the process  $0 \rightarrow \bar{u}d\nu_e e^+ H + g$  are provided in the Supplemental Material [26].

### C. Double-real emissions

The last ingredient for the NNLO computation comprises amplitudes for two real-emission processes  $0 \rightarrow \bar{u}d\nu_e e^+ H + gg$  and  $0 \rightarrow \bar{u}d\nu_e e^+ H + q\bar{q}$ . The calculation relies on the spinor-helicity methods and is completely straightforward. Amplitudes for the vector current  $\mathcal{H}_1^\mu$  can



be extracted from Refs. [59,60]; amplitudes for the  $\sigma^{\mu\nu} p_{W,\nu}$  current are new and are provided in the Supplemental Material [26].

#### D. Combining amplitudes

Ultraviolet-renormalized loop amplitudes contain  $1/\epsilon$  poles arising from soft and collinear virtual partons. Similarly, the real-emission amplitudes develop singularities when the emitted partons become soft or collinear to other partons. This implies that the real-emission amplitudes cannot be integrated over the full radiative phase space in four space-time dimensions. Removing the singularities arising from the real-emission corrections and combining them with those from the virtual corrections to arrive at an infrared-finite final result requires a subtraction scheme. For the calculations described in this paper, we employ the nested soft-collinear subtraction scheme [61,62], which has previously been used in several studies of  $VH$  phenomenology [14,22,63]. We note that since the infrared and collinear limits of the real-emission amplitudes are universal, upgrading the calculations reported in Refs. [14,22,63] to include the EFT contributions is straightforward since only hard, four-dimensional amplitudes have to be provided anew. Furthermore, the numerical code used in Refs. [14,22,63] and in other similar computations [59,60] is modular, allowing the implementation of the amplitudes discussed above in a straightforward way. To check the implementation, we confirmed that the subtraction terms have the same behavior as the amplitudes in the various unresolved limits and also that the SM results for  $W^+H$  production are reproduced [22,63].

#### IV. PHENOMENOLOGICAL RESULTS

In this section, we present phenomenological results through NNLO in perturbative QCD. We consider the process  $pp \rightarrow W^+(\rightarrow e^+\nu_e)H$  and remind the reader that, for the sake of simplicity, the Higgs is treated as a stable particle. We begin by listing the physical parameters and selection criteria used in the calculation.

We set the Higgs boson mass to  $m_H = 125$  GeV and the  $W$  boson mass to  $m_W = 80.399$  GeV. We use the Fermi constant  $G_F = 1.16639 \times 10^{-5}$  GeV $^{-2}$ , and the sine squared of the weak mixing angle  $\sin^2 \theta_W = 1 - m_W^2/m_Z^2$  with  $m_Z = 91.1876$  GeV. The width of the  $W$  boson is taken to be  $\Gamma_W = 2.1054$  GeV. Furthermore, we take the SMEFT scale  $\Lambda$  to be 1 TeV. Finally, we treat the decay process  $W^+ \rightarrow \nu_e e^+$  in the narrow-width approximation. Using the above parameters, the branching ratio evaluates to  $\text{Br}(W \rightarrow \nu_e e^+) = 0.10801$ .

To present numerical results we employ the parton distribution function (PDF) set NNPDF31\_nnlo\_as\_0118. We use NNLO PDFs to compute LO, NLO and NNLO cross sections in what follows. The values of the strong coupling constant  $\alpha_s$  are obtained from the NNPDF

routines. We choose  $\mu = \mu_R = \mu_F = \sqrt{(p_{W^+} + p_H)^2}/2$  as central renormalization/factorization scale for the production process, and estimate uncertainties related to higher-order QCD effects by varying the scale by a factor of two in either direction.

In order to keep our analysis as broad as possible, we apply very loose kinematic cuts to define the fiducial phase space. We require that the transverse momentum of the positron originating from the  $W^+$  decay is  $p_{T,e^+} > 25$  GeV, and its rapidity satisfies  $|\eta_{e^+}| < 2.5$ . In order to ensure the kinematic regime in which SMEFT is applicable, we further require that the  $W^+$ -boson transverse momentum satisfies  $p_{T,W^+}^{\text{max}} < 250$  GeV. This cut does not completely exclude events with high invariant mass  $m_{W^+H}$ . However, at leading order for fixed high  $m_{W^+H}$ , the transverse momentum of the  $W$  boson is constrained to be  $p_{T,W^+} \lesssim m_{W^+H}/2$ . Hence, for  $m_{W^+H} > 542$  GeV, the fraction of  $W$ -bosons that pass the cut decreases with the increase of  $m_{W^+H}$ . Together with the decreasing parton flux at high Bjorken  $x$ , this leads to a significant suppression of high invariant mass contributions and ensures the applicability of SMEFT for our analyses. Furthermore, in  $WH$  studies, an additional cut  $p_{T,W^+} > 150$  GeV is sometimes imposed to emphasize the boosted Higgs contributions. In what follows we present results for fiducial cross sections with and without this cut.

The modified SM Lagrangian considered in this paper contains four dimension-six operators, see Eqs. (2), (4). As discussed in the previous section, these operators lead to scattering amplitudes characterized by different helicity selection rules for the external quarks. Only one of these operators,  $Q_{\phi q}^{(3)}$ , leads to an amplitude that interferes with the SM one, whereas the contributions of all other operators interfere neither with the SM, nor with each other. This feature remains true through NNLO in QCD. Consequently, in the context of the SM extension discussed in this paper, one can write the most general differential cross section as the sum of six terms weighted with the corresponding coefficients

$$d\sigma = d\sigma_{\text{SM}} + C_{uW}^2 d\sigma_{uW} + C_{dW}^2 d\sigma_{dW} + C_{\phi q}^{(3)} d\sigma_I + (C_{\phi q}^{(3)})^2 d\sigma_{\phi q^{(3)}} + C_{\phi ud}^2 d\sigma_{\phi ud}. \quad (39)$$

We obtain the cross sections<sup>7</sup>  $d\sigma_{uW}$ ,  $d\sigma_{dW}$ ,  $d\sigma_{\phi q^{(3)}}$ , and  $d\sigma_{\phi ud}$  by setting the associated coupling coefficient to one and all other contributions, including that of the SM, to zero. To obtain the interference term  $d\sigma_I$ , we take the difference between the calculation that yields  $d\sigma_{\phi q^{(3)}}$  and a

<sup>7</sup>It is not quite proper to call these six contributions “cross sections” since one of them is the interference and, therefore, does not have to be positive-definite, but we will do this nonetheless.

TABLE I. Fiducial cross sections (in fb) at LO, NLO and NNLO for  $pp \rightarrow W^+(\rightarrow \nu_e e^+)H$  production at the 13 TeV LHC. The subscripts indicate the maximum and minimum values obtained by varying the factorization/renormalization by a factor of two in either direction. The fifth and sixth columns show the NLO and NNLO  $k$ -factors. Statistical errors are below the displayed digit, and are not shown. The table below is derived with an additional cut  $p_{T,W^+} > 150$  GeV. See text for details.

<i>Fiducial cross sections at LO, NLO, and NNLO</i>					
<i>Case</i>	$\sigma_{\text{LO}}$	$\sigma_{\text{NLO}}$	$\sigma_{\text{NNLO}}$	$k_{\text{NLO}}$	$k_{\text{NNLO}}$
SM	$47.84^{+1.65}_{-2.10}$	$58.12^{+0.59}_{-0.26}$	$58.61^{+0.08}_{-0.06}$	1.215	1.008
$uW$	$59.35^{+0.56}_{-0.93}$	$79.98^{+4.14}_{-3.31}$	$83.14^{+3.85}_{-3.22}$	1.347	1.040
$dW$	$38.98^{+0.36}_{-0.61}$	$52.96^{+2.78}_{-2.23}$	$55.17^{+2.58}_{-2.17}$	1.358	1.042
$\phi q^{(3)}$	$58.65^{+0.59}_{-0.97}$	$69.74^{+0.96}_{-0.61}$	$70.12^{+0.08}_{-0.03}$	1.189	1.006
$I$	$88.47^{+2.10}_{-2.80}$	$106.1^{+1.21}_{-0.64}$	$106.8^{+0.25}_{-0.11}$	1.200	1.007
$\phi ud$	$16.13^{+0.16}_{-0.27}$	$19.11^{+0.24}_{-0.15}$	$19.20^{+0.01}_{-0.01}$	1.185	1.005
<i>Fiducial cross sections at LO, NLO, and NNLO (<math>p_{T,W^+} &gt; 150</math> GeV)</i>					
<i>Case</i>	$\sigma_{\text{LO}}$	$\sigma_{\text{NLO}}$	$\sigma_{\text{NNLO}}$	$k_{\text{NLO}}$	$k_{\text{NNLO}}$
SM	$6.357^{+0.021}_{-0.057}$	$8.121^{+0.191}_{-0.139}$	$8.314^{+0.040}_{-0.050}$	1.278	1.024
$uW$	$30.46^{+0.02}_{-0.15}$	$40.82^{+2.26}_{-1.81}$	$42.39^{+1.92}_{-1.62}$	1.340	1.039
$dW$	$20.65^{+0.02}_{-0.11}$	$27.83^{+1.57}_{-1.25}$	$28.94^{+1.33}_{-1.12}$	1.348	1.040
$\phi q^{(3)}$	$30.54^{+0.00}_{-0.13}$	$36.03^{+0.58}_{-0.41}$	$36.23^{+0.04}_{-0.05}$	1.180	1.006
$I$	$26.22^{+0.04}_{-0.14}$	$31.61^{+0.54}_{-0.39}$	$31.89^{+0.10}_{-0.14}$	1.204	1.010
$\phi ud$	$8.065^{+0.004}_{-0.040}$	$9.501^{+0.147}_{-0.106}$	$9.552^{+0.003}_{-0.014}$	1.178	1.005

similar calculation in which the SM coupling is not removed.

We begin by discussing the different contributions to Eq. (39). In Table I, we present the fiducial cross sections for the quantities defined there at LO, NLO and NNLO, without and with the cut  $p_{T,W^+} > 150$  GeV. A striking feature of these results is that the cross sections associated with SMEFT operators are large: they are comparable to the SM cross sections for basic fiducial cuts, but start exceeding it if, in addition, the  $p_{T,W^+} > 150$  GeV cut is applied. We note that this cut effectively increases the invariant mass of the  $W^+H$  final states that contribute to the corresponding cross sections.

Given the large cross sections arising from the SMEFT operators, it is clear that most combinations of  $\mathcal{O}(1)$  coefficients can be excluded very quickly, negating the need for higher order corrections. However, the values in Table I together with Eq. (39) allow one to compute the cross section for *any* combination of values of the Wilson coefficients, including those which are far more challenging to constrain using experimental data. Indeed, Eq. (39) suggests that this can be done not only at the level of fiducial cross sections but also for differential distributions. We will return to this point later.

It is to be expected that cross sections driven by SMEFT operators contribute more at higher invariant masses because of their high mass dimension. However, in the current case there is another mechanism that enhances their contributions, namely the fact that the SM amplitude

contains an intermediate  $W^+$  boson propagator in the  $s$ -channel, whereas SMEFT contributions lead to a *direct* transition from a  $q\bar{q}$  initial state to the  $W^+H$  final state. Since the  $W^+$  boson propagator decreases when the invariant mass of the  $W^+H$  system increases, the SM contribution gets suppressed rapidly in comparison to the contribution of SMEFT operators. This point is clearly seen in the normalized  $W^+H$  invariant mass distribution shown in Fig. 4 where the very different shapes of the SM and SMEFT contributions are apparent.

To understand this better, we can estimate the dependence of the relevant amplitudes on the invariant mass of the  $WH$  system. Writing the weak coupling as  $g \sim m_W/v$ , we find

$$|\mathcal{M}_{\text{SM}}|^2 \sim \frac{m_W^4 m_{WH}^4}{(m_{WH}^2 - m_W^2)^2 v^4}, \quad |\mathcal{M}_{\text{SMEFT}}|^2 \sim \frac{m_{WH}^4}{\Lambda^4}. \quad (40)$$

Hence, taking  $m_{WH} \sim 300$  GeV, we find that the SMEFT amplitude is comparable to the SM one. We emphasize, however, that the energy scale  $m_{WH} \sim 300$  GeV should be safe for the SMEFT expansion since it is well below the SMEFT energy scale  $\Lambda = 1$  TeV.

Since the SM and the SMEFT cross sections receive contributions from rather different values of the  $W^+H$  invariant mass, their QCD corrections cannot be expected to be similar *a priori*. In fact, as can be seen from Table I, this is indeed not the case. The NLO QCD corrections increase the fiducial cross sections for the SM and a few of

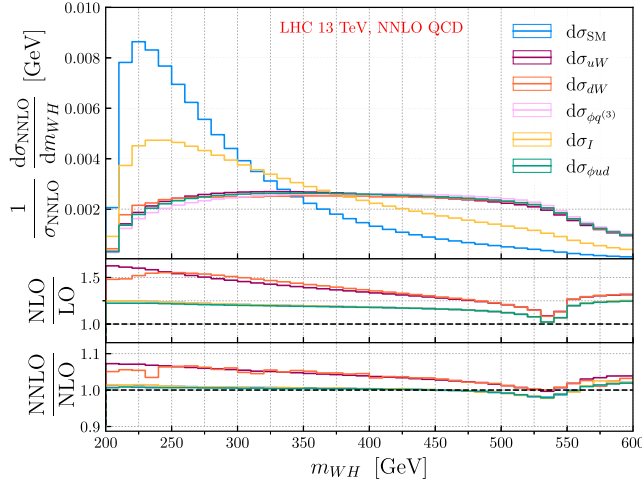


FIG. 4. Normalized distribution of the invariant mass of the  $W^+H$  system in  $pp \rightarrow W^+(\rightarrow \nu_e e^+)H$  at the 13 TeV LHC, for the six differential cross sections defined in Eq. (39). The upper pane shows the results at NNLO in QCD. The middle and lower panes show the NLO/LO and NNLO/NLO differential  $k$ -factors, respectively. Only the curves for the central factorization/renormalization scale are shown. See text for further details.

the SMEFT operators by  $\mathcal{O}(20\%)$ , but lead to a stronger  $\mathcal{O}(35\%)$  increase for the two  $CP$ -odd operators  $Q_{uW}$  and  $Q_{dW}$ . An additional cut  $p_{T,W^+} > 150$  GeV does not change the NLO corrections significantly, other than for the SM case, where they increase to 28%. The NLO QCD corrections are not captured by the scale variation, which amounts to 1%–5% only for the six cross sections that we consider. This underestimation of NLO corrections is a common feature of Drell-Yan like processes, due in part to the opening of new channels at NLO and the absence of an  $\alpha_s(\mu_R)$  dependence at LO.

Turning now to the NNLO corrections, we observe an increase in the values  $\sigma_{uW}$  and  $\sigma_{dW}$  by 4%, largely

independent of the presence of the  $p_{T,W^+}$  cut. For the other coupling scenarios and for the central renormalization and factorization scales, the NNLO corrections amount to less than a percent with the standard fiducial cuts, and between 1% and 2% with the additional  $p_{T,W^+}$  cut. These are captured by the scale uncertainties at NLO, and we note that the NLO uncertainties for  $\sigma_{uW}$  and  $\sigma_{dW}$  are larger than for the other cross sections, reflecting their larger NNLO corrections. At NNLO, the scale variations are around 5% for these two quantities, but are at or below the percent level for the four other cross sections displayed in Table I.

It is also interesting to understand how the higher order QCD corrections affect the zero-jet and the one-jet bins. This is especially relevant given that jet-binned simplified template cross sections (STXS) are an essential aspect of most analysis strategies at the LHC. In Table II, we present the fiducial cross sections in the boosted regime  $p_{T,W^+} > 150$  GeV, split into the exclusive zero-jet and inclusive one-jet bins, where jets are defined using the anti- $k_T$  algorithm [64] with  $\Delta R = 0.4$  and are required to have  $p_T > 20$  GeV. We note that our results have only NLO accuracy in the inclusive one-jet bin, although NNLO results for  $WH + j$  production in the SM are known [65,66]. We observe that the ratio of the zero-jet rate to the LO rate is quite similar for all coupling options considered, ranging between 0.58 and 0.62 at NLO and between 0.54 and 0.57 at NNLO. Hence, although the NLO corrections reduce the zero-jet rate significantly, the NNLO calculation stabilizes it. Furthermore, this also implies that the additional radiation at NLO strongly populates the 1-jet inclusive bins. To illustrate this, we display the emission ratios  $E_{\text{NLO}}$  and  $E_{\text{NNLO}}$ , defined as

$$E_i = \frac{\sigma_i^{(\geq 1 \text{ jet})}}{\sigma_i^{(0 \text{ jet})}}, \quad i = \text{NLO, NNLO}, \quad (41)$$

TABLE II. Jet-binned fiducial cross sections (in fb) at NLO and NNLO for  $pp \rightarrow W^+(\rightarrow \nu_e e^+)H$  production at the 13 TeV LHC, including the cut  $p_{T,W^+} > 150$  GeV. The subscripts indicate the maximum and minimum values obtained by varying the factorization/renormalization scale by a factor of two in either direction. The sixth and seventh columns show the ratio of the inclusive one-jet bin to the zero-jet bin at NLO and NNLO, respectively. See text for details.

Jet-binned fiducial cross sections at NLO and NNLO ( $p_{T,W^+} > 150$ GeV)						
Case	0 jet	1 jet	0 jet	$\geq 1$ jet	$E_{\text{NLO}}$	$E_{\text{NNLO}}$
	$\sigma_{\text{NLO}}$		$\sigma_{\text{NNLO}}$			
SM	$3.897^{+0.294}_{-0.328}$	$4.227^{+0.518}_{-0.436}$	$3.583^{+0.072}_{-0.041}$	$4.743^{+0.073}_{-0.128}$	1.08	1.32
$uW$	$18.95^{+0.60}_{-0.63}$	$21.87^{+2.89}_{-2.42}$	$17.23^{+0.51}_{-0.27}$	$25.17^{+1.370}_{-1.377}$	1.15	1.46
$dW$	$12.82^{+0.41}_{-0.42}$	$15.01^{+1.98}_{-1.66}$	$11.68^{+0.35}_{-0.22}$	$17.27^{+0.94}_{-0.93}$	1.17	1.48
$\phi q^{(3)}$	$17.98^{+1.51}_{-1.74}$	$18.06^{+2.31}_{-1.93}$	$16.46^{+0.38}_{-0.17}$	$19.79^{+0.19}_{-0.46}$	1.00	1.20
$I$	$15.76^{+1.29}_{-1.38}$	$15.82^{+1.94}_{-1.65}$	$14.43^{+0.34}_{-0.05}$	$17.46^{+0.21}_{-0.43}$	1.00	1.21
$\phi ud$	$4.775^{+0.401}_{-0.455}$	$4.726^{+0.605}_{-0.506}$	$4.359^{+0.109}_{-0.038}$	$5.187^{+0.051}_{-0.116}$	0.99	1.19

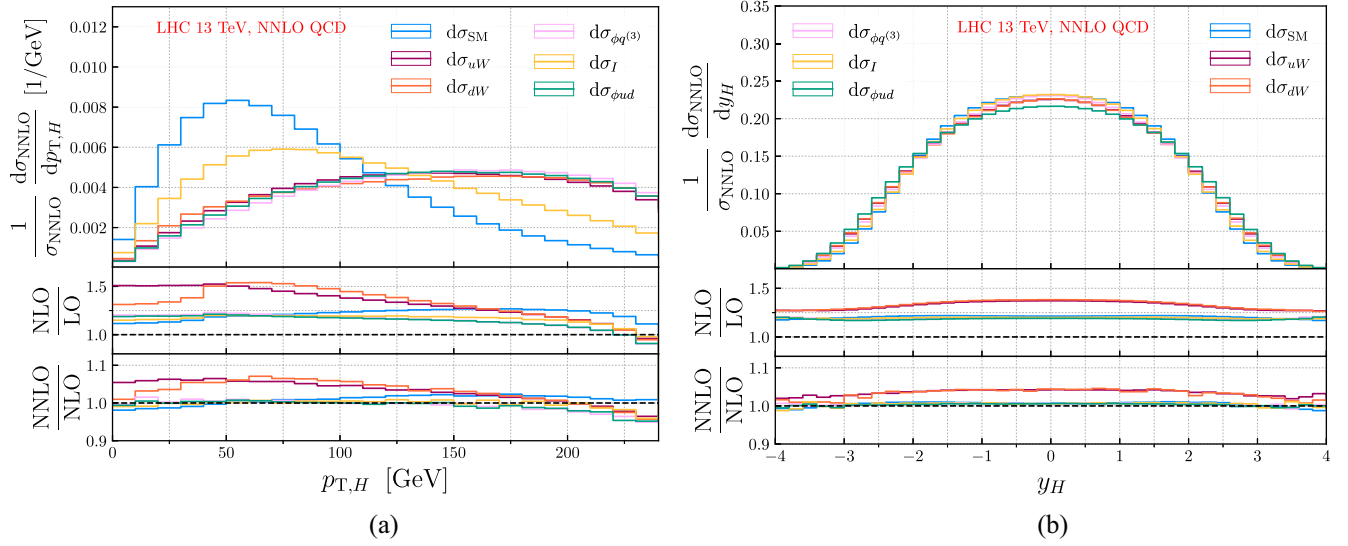


FIG. 5. As for Fig. 4 but displaying the normalized distributions of the transverse momentum (a) and rapidity (b) of the Higgs boson.

in the sixth and seventh columns of Table II. These ratios notably increase from NLO to NNLO indicating that more and more events have additional radiation. This ratio is largest for  $\sigma_{uW}$  and  $\sigma_{dW}$ , both at NLO and at NNLO, amounting to close to 1.5 in the latter, meaning that roughly three out of every five events would be accompanied by at least one hard jet. The values for  $\sigma_{SM}$  are somewhat smaller but still indicate that a substantial fraction of  $W^+H$  events are produced with jets. Interestingly, the ratios for  $\sigma_{\phi q^{(3)}}$ ,  $\sigma_{\phi ud}$  and  $\sigma_I$  are close to one at NLO, but jump significantly to around 1.20 at NNLO.

These differences in the various fiducial cross sections also get reflected in how QCD corrections affect the kinematic distributions. Since we are chiefly interested in the shape differences between distributions for different SMEFT operators, and the impact of QCD corrections on them, we normalize all distributions to their NNLO cross section, so that the area under each curve is unity. We also display results for the central scale only, in order to keep the plots as uncluttered as possible.

The NLO and NNLO QCD corrections to the  $W^+H$  invariant mass distribution are shown in Fig. 4, which we mentioned above. Looking at the lower two panels of this figure, we can see that the NLO corrections for the quantities  $d\sigma_{uW}$  and  $d\sigma_{dW}$  start off very large, enhancing the cross section by around 50% for  $m_{W^+H} \approx 200$  GeV, and then decrease to about 10%, before beginning to increase again for  $m_{W^+H} \gtrsim 540$  GeV. By contrast, the  $k$ -factors for the other differential cross sections are relatively flat, although they each reach a minimum at the same value  $m_{W^+H} \approx 540$  GeV and increase for larger values of the invariant mass. To understand the existence of this minimum, recall that our cut  $p_{T,W^+} < 250$  GeV suppresses events with  $m_{W^+H} \gtrsim 540$  GeV at LO. However, such

events become more abundant at higher orders as the  $W$  boson can recoil against radiated partons. In general, the NNLO  $k$ -factor has a similar although less pronounced pattern compared to the NLO one.

In Fig. 5, we show the transverse momentum and the rapidity of the Higgs boson. We observe a significant shape difference in the  $p_{T,H}$  distribution between the SM and SMEFT results. However, the different SMEFT operators lead to very similar shapes of this distribution. On the contrary, the QCD corrections do depend on the SMEFT operator that mediates the  $W^+H$  production. At NLO, the corrections to  $d\sigma_{uW}$  start off large and then decrease, becoming negative for  $p_{T,H} \gtrsim 230$  GeV. The corrections to  $d\sigma_{dW}$  increase at small  $p_{T,H}$ , reaching a maximum value of about 50% at  $p_{T,H} \approx 60$  GeV and then decrease. In contrast, the corrections to the SM have a very slow increase with  $p_{T,H}$  over most of the values considered. Again, these patterns persist at NNLO, although the effects are much milder there. The shape of the Higgs boson rapidity distribution is largely insensitive to the production mechanism, and we have checked that this is true for other rapidities, e.g., that of the positron. Furthermore, for all rapidity observables, the differential  $k$ -factors are largely constant and similar to the  $k$ -factors of the fiducial cross sections shown in Table I.

We turn to Fig. 6, where we show the transverse momentum of the positron and the missing transverse momentum. Looking at the upper row, it is clear that these observables have different shapes for the different SMEFT operators, except for  $d\sigma_{\phi q^{(3)}}$  and  $d\sigma_{\phi ud}$ . The  $k$ -factors for  $p_{T,e^+}$  are quite flat at NLO and NNLO, except for  $k_{SM}$  at NLO which increases from around 1.2 at low  $p_{T,e^+}$  to almost 1.4 at  $p_{T,e^+} = 200$  GeV. The differential  $k$ -factors for  $p_{T,miss}$  have a very similar behavior, at



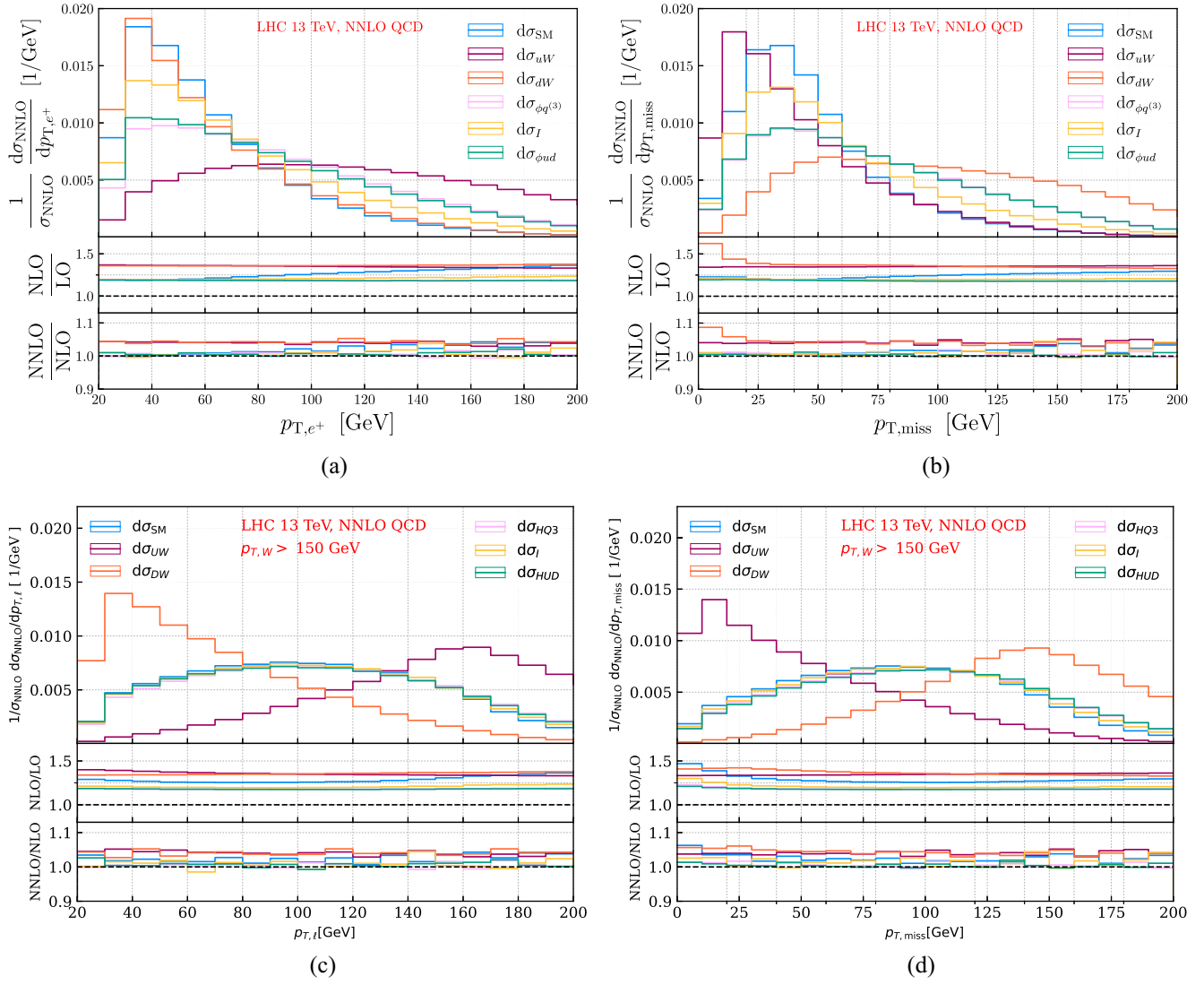


FIG. 6. As for Fig. 4 but displaying the normalized distributions for the transverse momentum of the positron (a) and (c) and the missing transverse momentum (b) and (d). The plots on the lower row include an additional cut  $p_{T,W^+} > 150$  GeV. See main text for details.

least in the region of phase space where the bulk of events lies.

It is also interesting to study these leptonic observables in the presence of the cut on the  $W$  boson transverse momentum,  $p_{T,W^+} > 150$  GeV, which we show in the lower row of Fig. 6. We observe that the presence of the cut causes the  $p_{T,\ell}$  distributions to become significantly harder for all contributions except for  $d\sigma_{dW}$ , while  $p_{T,\text{miss}}$  becomes harder for every contribution except for  $d\sigma_{uW}$ . While this makes it harder to distinguish between the SM shape and those from  $d\sigma_{\phi ud}$  and  $d\sigma_{\phi q^{(3)}}$ , it also suggests that boosted kinematics may be especially helpful in probing the coefficients  $C_{uW}$  and  $C_{dW}$ .<sup>8</sup> The impact of the higher

order corrections do change somewhat due to the  $p_{T,W^+}$  cut, e.g. the corrections in the  $d\sigma_{\text{SM}}$  distributions at low  $p_{T,\text{miss}}$  become stronger. However, these changes occur in regions of phase space which are less populated as a consequence of the  $p_{T,W^+}$  cut.

Using associated  $WH$  production to search for deviations from the SM within the SMEFT framework involves comparing data with theoretical predictions for many values of the Wilson coefficients. It may appear that performing such a comparison with NNLO accuracy for many combinations of SMEFT couplings is a daunting task, given the complexity of NNLO computations, but this is not necessarily the case, as we now explain. Indeed, since we can write the most general cross section for  $W^+H$  production as the sum of six terms [cf. in Eq. (39)], it is clear that once individual *differential* cross sections are calculated, one can easily sum them up including their

<sup>8</sup>We note that other processes, e.g.,  $Z + \text{jet}$  production, are also sensitive to these coefficients.



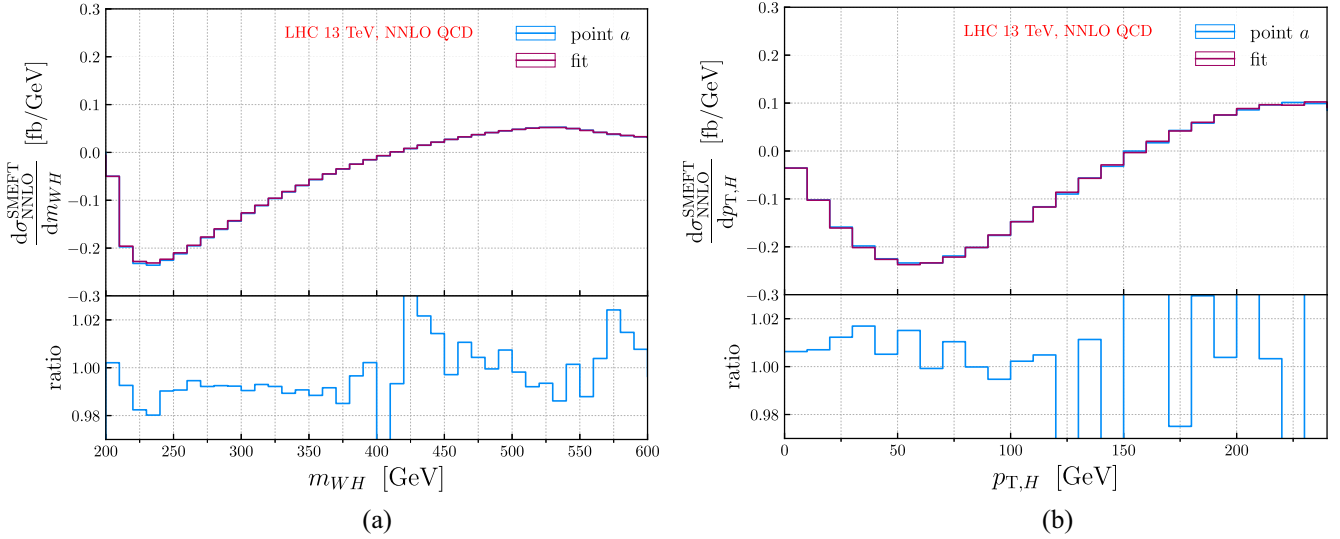


FIG. 7. Exact calculation of the difference between the SMEFT and SM results for the invariant mass distribution of the  $W^+H$  system (a) and the transverse momentum of the Higgs boson (b) compared with distributions obtained using a fit [cf., Eq. (39)]. Distributions are obtained using the central factorization/renormalization scale, and the fiducial cuts described in the main text.

respective Wilson coefficients and obtain any kinematic distribution for *arbitrary* combinations of SMEFT couplings on the fly. To test the quality of this procedure, we have chosen a random set of Wilson coefficients

$$(a): C_{uW} = 0.321, \quad C_{dW} = 0.521, \\ C_{\phi q}^{(3)} = -0.718, \quad C_{\phi ud} = 0.451, \quad (42)$$

and evaluated the cross sections to NNLO accuracy by integrating matrix elements squared with all Wilson coefficients included. We then compared this result with the cross section that is reconstructed from the individual “cross sections” using Eq. (39) and found agreement below the permille level for the fiducial cross section using the cuts described above. At a differential level, it is most important to study the *difference*  $d\Delta_{\text{NNLO}}^{\text{SMEFT}}$  between the SM and the SMEFT result using this procedure. In Fig. 7, we display  $d\Delta_{\text{NNLO}}^{\text{SMEFT}}$  for the invariant mass distribution of the  $W^+H$  system,  $m_{W^+H}$ , and the transverse momentum of the Higgs boson,  $p_{T,H}$ . We see that Eq. (39) reproduces these differences with around percent-level precision across a large range of values of the observables (except where the SMEFT and the SM distributions practically coincide), indicating that the numerical uncertainties are well-controlled. This suggests the following strategy: one computes the SM results to a given higher-order accuracy, and then one combines these with SMEFT results generated for a wide range of couplings, at essentially zero computational cost. Since NNLO accuracy is most relevant when the impact of the SMEFT operators is small, this strategy may open up an opportunity to perform scans that include multiple Wilson coefficients efficiently.

## V. CONCLUSION

In this paper, we have studied the impact of dimension-six SMEFT operators on the associated Higgs boson production  $pp \rightarrow W^+H$  at the LHC. We have calculated the NNLO QCD corrections to this process for SMEFT-initiated contributions. Although such computations are quite straightforward by now, they still require some effort. For example, the so-called  $CP$ -odd SMEFT operators introduce pointlike interactions  $q\bar{q}'WH$  which are facilitated by a tensor  $(\sigma^{\mu\nu} p_{W,\nu})$  current, for which two-loop amplitudes are not known. Therefore, studying contributions of such operators to  $pp \rightarrow W^+H$  production with NNLO QCD accuracy requires a dedicated computation of new two- and one-loop amplitudes.

Due to helicity selection rules, amplitudes facilitated by these  $CP$ -odd SMEFT operators do not interfere with the Standard Model ones. As the result, only their squares contribute to  $pp \rightarrow W^+H$  cross sections, thereby leading to a stronger suppression by the SMEFT energy scale. Nevertheless, we find that contributions of these operators are quite substantial, and that QCD corrections to cross sections induced by these operators are significant and sometimes different from similar corrections in the SM.

We also find that kinematic distributions show varying degrees of sensitivity to the different production mechanisms, with the Higgs boson rapidity distribution being the most insensitive. What is also important is that the QCD corrections are not uniform for different SMEFT operators. This is especially true at NLO, whereas the remaining differences at NNLO are significantly less dramatic.

It is clear that the large cross sections induced by the SMEFT operators, as well as the difference in the shapes of the  $m_{W^+H}$  and  $p_{T,H}$  distributions, provide valuable

information which should help to place stringent bounds on relevant Wilson coefficients. Although, based on experience with SM calculations, one can argue that the scale variation at NLO in cases with SM-like corrections reasonably captures the magnitude of NNLO QCD effects, the same arguments could not be made for  $d\sigma_{uW}$  and  $d\sigma_{dW}$  previously, since both the size of the NLO QCD corrections as well as the range of  $WH$  invariant masses which provides the main contribution are different. Hence, to establish the perturbative stability of large NLO effects, the complete NNLO QCD computation was required. We have provided such an analysis in this paper and look forward to its future usage for experimental studies of  $W^+H$  production in the context of SMEFT.

### ACKNOWLEDGMENTS

M. B. wishes to thank Federico Buccioni, Federica Devoto, Magnus Schaaf, Chiara Signorile-Signorile, Lukas Simon, and Hantian Zhang for support and fruitful discussions during different stages of this work. M.-M. L. expresses gratitude to Marius Höfer for beneficial conversations and help with GoSam. D. M. T. and R. R. are grateful to the Institute for Theoretical Particle Physics at KIT for hospitality extended to them during the course of the work on this paper. R. V. H. would like to thank Anke Biekötter and Tom Tong for helpful conversations. This work is supported by the Italian Ministry of Universities and Research (MUR) through Grant No. PRIN 2022BCXSW9 and the *Deutsche Forschungsgemeinschaft* (DFG, German Research Foundation) under Grant No. 396021762—TRR 257. All Feynman diagrams in this paper are produced by FeynGame [67–69].

### DATA AVAILABILITY

The data that support the findings of this article are not publicly available. The data are available from the authors upon reasonable request.

### APPENDIX: INFRARED BEHAVIOR OF THE AMPLITUDES

The renormalized virtual NLO and NNLO amplitudes contain only IR divergences, which manifest themselves as poles in the dimensional regularization parameter  $\epsilon$ . These IR singularities are universal and are described by Catani's formula [50]

$$\begin{aligned}\tilde{\mathcal{M}}^{(1)} &= \mathbf{I}^{(1)}\tilde{\mathcal{M}}^{(0)} + \tilde{\mathcal{M}}^{(1),\text{finite}}, \\ \tilde{\mathcal{M}}^{(2)} &= \mathbf{I}^{(2)}\tilde{\mathcal{M}}^{(0)} + \mathbf{I}^{(1)}\tilde{\mathcal{M}}^{(1)} + \tilde{\mathcal{M}}^{(2),\text{finite}},\end{aligned}\quad (\text{A1})$$

where  $\tilde{\mathcal{M}}$  indicates the renormalized  $0 \rightarrow \bar{u}d\nu_e e^+ H$  amplitude, and the operators  $\mathbf{I}^{(1,2)}$  read

$$\begin{aligned}\mathbf{I}^{(1)}(p_1, p_2; \epsilon) &= -C_\epsilon C_F \left( \frac{2}{\epsilon^2} + \frac{3}{\epsilon} \right) \eta_{12}, \\ \mathbf{I}^{(2)}(p_1, p_2; \epsilon) &= -\frac{[\mathbf{I}^{(1)}(p_1, p_2; \epsilon)]^2}{2} - \frac{\beta_0}{\epsilon} \mathbf{I}^{(1)}(p_1, p_2; \epsilon) \\ &\quad + e^{-\epsilon\gamma_E} \frac{\Gamma(1-2\epsilon)}{\Gamma(1-\epsilon)} \left( \frac{\beta_0}{\epsilon} + \mathbf{K} \right) \mathbf{I}^{(1)}(p_1, p_2; 2\epsilon) \\ &\quad + \mathbf{H}^{(2)}(p_1, p_2; \epsilon),\end{aligned}\quad (\text{A2})$$

with

$$\begin{aligned}C_\epsilon &= \frac{e^{\epsilon\gamma_E}}{2\Gamma(1-\epsilon)}, \quad \mathbf{K} = \left( \frac{67}{18} - \frac{\pi^2}{6} \right) C_A - \frac{10}{9} n_f T_R, \\ \eta_{ij} &= \left( -\frac{\mu^2}{s_{ij}} \right)^\epsilon,\end{aligned}\quad (\text{A3})$$

and [70,71]

$$\begin{aligned}\mathbf{H}^{(2)}(p_1, p_2; \epsilon) &= \frac{C_\epsilon C_F}{\epsilon} \left[ \left( \frac{13\zeta_3}{2} - \frac{23\pi^2}{48} + \frac{245}{216} \right) C_A \right. \\ &\quad \left. + \left( -6\zeta_3 + \frac{\pi^2}{2} - \frac{3}{8} \right) C_F + \left( \frac{\pi^2}{12} - \frac{25}{54} \right) n_f T_R \right].\end{aligned}\quad (\text{A4})$$

The IR structure of the renormalized real-virtual amplitude is described by Catani's formula as well. In this case, the decomposition reads

$$\tilde{\mathcal{M}}^{(1)} = \mathbf{I}^{(1)}\tilde{\mathcal{M}}^{(0)} + \tilde{\mathcal{M}}^{(1),\text{finite}},\quad (\text{A5})$$

where

$$\begin{aligned}\mathbf{I}^{(1)}(p_1, p_2, p_3; \epsilon) &= C_\epsilon \left[ (C_A - 2C_F) \left( \frac{1}{\epsilon^2} + \frac{3}{2\epsilon} \right) \eta_{12} \right. \\ &\quad \left. - \left( \frac{C_A}{\epsilon^2} + \frac{3C_A}{4\epsilon} + \frac{\beta_0}{2\epsilon} \right) (\eta_{15} + \eta_{25}) \right].\end{aligned}\quad (\text{A6})$$

We explicitly verify that the IR structure of the amplitudes computed in Sec. III agrees with Eqs. (A1) and (A5).

- [1] R. L. Workman *et al.* (Particle Data Group), Review of particle physics, *Prog. Theor. Exp. Phys.* **2022**, 083C01 (2022).
- [2] S. Weinberg, Baryon and lepton nonconserving processes, *Phys. Rev. Lett.* **43**, 1566 (1979).
- [3] W. Buchmüller and D. Wyler, Effective Lagrangian analysis of new interactions and flavor conservation, *Nucl. Phys.* **B268**, 621 (1986).
- [4] B. Grzadkowski, M. Iskrzynski, M. Misiak, and J. Rosiek, Dimension-six terms in the standard model Lagrangian, *J. High Energy Phys.* **10** (2010) 085.
- [5] R. Alonso, E. E. Jenkins, A. V. Manohar, and M. Trott, Renormalization group evolution of the standard model dimension six operators III: Gauge coupling dependence and phenomenology, *J. High Energy Phys.* **04** (2014) 159.
- [6] B. Henning, X. Lu, T. Meila, and H. Murayama, 2, 84, 30, 993, 560, 15456, 11962, 261485,...: Higher dimension operators in the SM EFT, *J. High Energy Phys.* **08** (2017) 016; **09** (2019) 19.
- [7] R. V. Harlander, T. Kempkens, and M. C. Schaaf, Standard model effective field theory up to mass dimension 12, *Phys. Rev. D* **108**, 055020 (2023).
- [8] J. M. Butterworth, A. R. Davison, M. Rubin, and G. P. Salam, Jet substructure as a new Higgs search channel at the LHC, *Phys. Rev. Lett.* **100**, 242001 (2008).
- [9] R. V. Harlander, J. Klappert, C. Pandini, and A. Papaefstathiou, Exploiting the  $WH/ZH$  symmetry in the search for new physics, *Eur. Phys. J. C* **78**, 760 (2018).
- [10] G. Ferrera, M. Grazzini, and F. Tramontano, Associated  $WH$  production at hadron colliders: A fully exclusive QCD calculation at NNLO, *Phys. Rev. Lett.* **107**, 152003 (2011).
- [11] G. Ferrera, M. Grazzini, and F. Tramontano, Higher-order QCD effects for associated  $WH$  production and decay at the LHC, *J. High Energy Phys.* **04** (2014) 039.
- [12] G. Ferrera, M. Grazzini, and F. Tramontano, Associated  $ZH$  production at hadron colliders: The fully differential NNLO QCD calculation, *Phys. Lett. B* **740**, 51 (2015).
- [13] J. M. Campbell, R. K. Ellis, and C. Williams, Associated production of a Higgs boson at NNLO, *J. High Energy Phys.* **06** (2016) 179.
- [14] F. Caola, G. Luisoni, K. Melnikov, and R. Rötsch, NNLO QCD corrections to associated  $WH$  production and  $H \rightarrow b\bar{b}$  decay, *Phys. Rev. D* **97**, 074022 (2018).
- [15] G. Ferrera, G. Somogyi, and F. Tramontano, Associated production of a Higgs boson decaying into bottom quarks at the LHC in full NNLO QCD, *Phys. Lett. B* **780**, 346 (2018).
- [16] R. Gauld, A. Gehrmann-De Ridder, E. W. N. Glover, A. Huss, and I. Majer, Associated production of a Higgs boson decaying into bottom quarks and a weak vector boson decaying leptonically at NNLO in QCD, *J. High Energy Phys.* **10** (2019) 002.
- [17] M. L. Ciccolini, S. Dittmaier, and M. Krämer, Electroweak radiative corrections to associated  $WH$  and  $ZH$  production at hadron colliders, *Phys. Rev. D* **68**, 073003 (2003).
- [18] A. Denner, S. Dittmaier, S. Kallweit, and A. Mück, Electroweak corrections to Higgs-strahlung off  $W/Z$  bosons at the Tevatron and the LHC with HAWK, *J. High Energy Phys.* **03** (2012) 075.
- [19] A. Denner, S. Dittmaier, S. Kallweit, and A. Mück, HAWK 2.0: A Monte Carlo program for Higgs production in vector-boson fusion and Higgs strahlung at hadron colliders, *Comput. Phys. Commun.* **195**, 161 (2015).
- [20] J. Baglio, C. Duhr, B. Mistlberger, and R. Szafron, Inclusive production cross sections at  $N^3LO$ , *J. High Energy Phys.* **12** (2022) 066.
- [21] S. Alioli, W. Dekens, M. Girard, and E. Mereghetti, NLO QCD corrections to SM-EFT dilepton and electroweak Higgs boson production, matched to parton shower in POWHEG, *J. High Energy Phys.* **08** (2018) 205.
- [22] W. Bizoń, F. Caola, K. Melnikov, and R. Rötsch, Anomalous couplings in associated  $VH$  production with Higgs boson decay to massive  $b$  quarks at NNLO in QCD, *Phys. Rev. D* **105**, 014023 (2022).
- [23] U. Haisch, D. J. Scott, M. Wiesemann, G. Zanderighi, and S. Zanolini, NNLO event generation for  $pp \rightarrow Zh \rightarrow \ell^+ \ell^- b\bar{b}$  production in the SM effective field theory, *J. High Energy Phys.* **07** (2022) 054.
- [24] R. Franceschini, G. Panico, A. Pomarol, F. Riva, and A. Wulzer, Electroweak precision tests in high-energy diboson processes, *J. High Energy Phys.* **02** (2018) 111.
- [25] R. Gauld, U. Haisch, and L. Schnell, SMEFT at NNLO + PS:  $Vh$  production, *J. High Energy Phys.* **01** (2024) 192.
- [26] See Supplemental Material at <http://link.aps.org/supplemental/10.1103/ct5x-hl46> for expressions for the two-loop, one-loop, and tree-level amplitudes used in this paper.
- [27] A. Dedes, W. Materkowska, M. Paraskevas, J. Rosiek, and K. Sucho, Feynman rules for the standard model effective field theory in  $R_\xi$ -gauge, *J. High Energy Phys.* **06** (2017) 143.
- [28] J. ter Hoeve, L. Mantani, A. N. Rossia, J. Rojo, and E. Vryonidou, Connecting scales: RGE effects in the SMEFT at the LHC and future colliders, *J. High Energy Phys.* **06** (2025) 125.
- [29] E. d. S. Almeida, A. Alves, O. J. P. Éboli, and M. C. Gonzalez-Garcia, Electroweak legacy of the LHC run II, *Phys. Rev. D* **105**, 013006 (2022).
- [30] J. Kley, T. Theil, E. Venturini, and A. Weiler, Electric dipole moments at one-loop in the dimension-6 SMEFT, *Eur. Phys. J. C* **82**, 926 (2022).
- [31] R. Boughezal, E. Mereghetti, and F. Petriello, Dilepton production in the SMEFT at  $O(1/\Lambda^4)$ , *Phys. Rev. D* **104**, 095022 (2021).
- [32] O. Brein, R. Harlander, M. Wiesemann, and T. Zirke, Top-quark mediated effects in hadronic Higgs-strahlung, *Eur. Phys. J. C* **72**, 1868 (2012).
- [33] B. A. Kniehl, Associated production of Higgs and  $Z$  bosons from gluon fusion in hadron collisions, *Phys. Rev. D* **42**, 2253 (1990).
- [34] O. Brein, A. Djouadi, and R. Harlander, NNLO QCD corrections to the Higgs-Strahlung processes at hadron colliders, *Phys. Lett. B* **579**, 149 (2004).
- [35] H. Elvang and Y.-t. Huang, Scattering amplitudes, [arXiv:1308.1697](https://arxiv.org/abs/1308.1697).
- [36] P. Nogueira, Automatic Feynman graph generation, *J. Comput. Phys.* **105**, 279 (1993).
- [37] B. Ruijl, T. Ueda, and J. Vermaseren, FORM version 4.2, [arXiv:1707.06453](https://arxiv.org/abs/1707.06453).
- [38] W. R. Inc., *Mathematica*, Version 13.0, Champaign, IL, 2024, <https://www.wolfram.com/mathematica>.
- [39] L. W. Garland, T. Gehrmann, E. W. N. Glover, A. Koukoutsakis, and E. Remiddi, Two loop QCD helicity

- amplitudes for  $e^+e^- \rightarrow$  three jets, *Nucl. Phys.* **B642**, 227 (2002).
- [40] T. Gehrmann, E. W. N. Glover, T. Huber, N. Ikizlerli, and C. Studerus, Calculation of the quark and gluon form factors to three loops in QCD, *J. High Energy Phys.* **06** (2010) 094.
- [41] K. G. Chetyrkin and F. V. Tkachov, Integration by parts: The algorithm to calculate  $\beta$  functions in 4 loops, *Nucl. Phys.* **B192**, 159 (1981).
- [42] S. Laporta, High-precision calculation of multiloop Feynman integrals by difference equations, *Int. J. Mod. Phys. A* **15**, 5087 (2000).
- [43] A. von Manteuffel and C. Studerus, Reduze 2—Distributed Feynman integral reduction, [arXiv:1201.4330](https://arxiv.org/abs/1201.4330).
- [44] P. Maierhöfer, J. Usovitsch, and P. Uwer, Kira—A Feynman integral reduction program, *Comput. Phys. Commun.* **230**, 99 (2018).
- [45] J. Klappert, F. Lange, P. Maierhöfer, and J. Usovitsch, Integral reduction with Kira 2.0 and finite field methods, *Comput. Phys. Commun.* **266**, 108024 (2021).
- [46] R. H. Lewis, Fermat: A computer algebra system for polynomial and matrix multiplication, computer Software, <https://home.bway.net/lewis>.
- [47] J. Klappert and F. Lange, Reconstructing rational functions with FireFly, *Comput. Phys. Commun.* **247**, 106951 (2020).
- [48] J. Klappert, S. Y. Klein, and F. Lange, Interpolation of dense and sparse rational functions and other improvements in FireFly, *Comput. Phys. Commun.* **264**, 107968 (2021).
- [49] T. Gehrmann and E. Remiddi, Differential equations for two loop four point functions, *Nucl. Phys.* **B580**, 485 (2000).
- [50] S. Catani, The singular behavior of QCD amplitudes at two loop order, *Phys. Lett. B* **427**, 161 (1998).
- [51] G. Passarino and M. J. G. Veltman, One loop corrections for  $e^+e^-$  annihilation into  $\mu^+\mu^-$  in the Weinberg model, *Nucl. Phys.* **B160**, 151 (1979).
- [52] F. Buccioni, J.-N. Lang, J. M. Lindert, P. Maierhöfer, S. Pozzorini, H. Zhang, and M. F. Zoller, OpenLoops 2, *Eur. Phys. J. C* **79**, 866 (2019).
- [53] J. Alwall, R. Frederix, S. Frixione, V. Hirschi, F. Maltoni, O. Mattelaer, H. S. Shao, T. Stelzer, P. Torrielli, and M. Zaro, The automated computation of tree-level and next-to-leading order differential cross sections, and their matching to parton shower simulations, *J. High Energy Phys.* **07** (2014) 079.
- [54] G. Cullen, N. Greiner, G. Heinrich, G. Luisoni, P. Mastrolia, G. Ossola, T. Reiter, and F. Tramontano (GoSam Collaboration), Automated one-loop calculations with GoSam, *Eur. Phys. J. C* **72**, 1889 (2012).
- [55] G. Cullen *et al.* (GoSam Collaboration), GoSam-2.0: A tool for automated one-loop calculations within the standard model and beyond, *Eur. Phys. J. C* **74**, 3001 (2014).
- [56] T. Peraro, FiniteFlow: Multivariate functional reconstruction using finite fields and dataflow graphs, *J. High Energy Phys.* **07** (2019) 031.
- [57] T. Gehrmann and E. Remiddi, Two loop master integrals for  $\gamma^* \rightarrow 3$  jets: The planar topologies, *Nucl. Phys.* **B601**, 248 (2001).
- [58] T. Gehrmann and E. Remiddi, Two loop master integrals for  $\gamma^* \rightarrow 3$  jets: The nonplanar topologies, *Nucl. Phys.* **B601**, 287 (2001).
- [59] O. Brein, R. V. Harlander, and T. J. E. Zirke, vh@nnlo—Higgs strahlung at hadron colliders, *Comput. Phys. Commun.* **184**, 998 (2013).
- [60] R. Boughezal, J. M. Campbell, R. K. Ellis, C. Focke, W. Giele, X. Liu, F. Petriello, and C. Williams, Color singlet production at NNLO in MCFM, *Eur. Phys. J. C* **77**, 7 (2017).
- [61] F. Caola, K. Melnikov, and R. Rötsch, Nested soft-collinear subtractions in NNLO QCD computations, *Eur. Phys. J. C* **77**, 248 (2017).
- [62] F. Caola, K. Melnikov, and R. Rötsch, Analytic results for color-singlet production at NNLO QCD with the nested soft-collinear subtraction scheme, *Eur. Phys. J. C* **79**, 386 (2019).
- [63] A. Behring, W. Bizoń, F. Caola, K. Melnikov, and R. Rötsch, Bottom quark mass effects in associated  $WH$  production with the  $H \rightarrow b\bar{b}$  decay through NNLO QCD, *Phys. Rev. D* **101**, 114012 (2020).
- [64] M. Cacciari, G. P. Salam, and G. Soyez, The anti- $k_t$  jet clustering algorithm, *J. High Energy Phys.* **04** (2008) 063.
- [65] R. Gauld, A. Gehrmann-De Ridder, E. Glover, A. Huss, and I. Majer, Precise predictions for  $WH + \text{jet}$  production at the LHC, *Phys. Lett. B* **817**, 136335 (2021).
- [66] R. Gauld, A. Gehrmann-De Ridder, E. W. N. Glover, A. Huss, and I. Majer,  $Vh + \text{jet}$  production in hadron-hadron collisions up to order  $\alpha_s^3$  in perturbative QCD, *J. High Energy Phys.* **03** (2022) 008.
- [67] R. V. Harlander, S. Y. Klein, and M. Lipp, FeynGame, *Comput. Phys. Commun.* **256**, 107465 (2020).
- [68] R. Harlander, S. Y. Klein, and M. C. Schaaf, FeynGame-2.1—Feynman diagrams made easy, *Proc. Sci. EPS-HEP2023* (2024) 657 [[arXiv:2401.12778](https://arxiv.org/abs/2401.12778)].
- [69] L. Bündgen, R. V. Harlander, S. Y. Klein, and M. C. Schaaf, FeynGame 3.0, *Comput. Phys. Commun.* **314**, 109662 (2025).
- [70] T. Becher and M. Neubert, On the structure of infrared singularities of gauge-theory amplitudes, *J. High Energy Phys.* **06** (2009) 081; **11** (2013) 24.
- [71] T. Becher and M. Neubert, Infrared singularities of scattering amplitudes in perturbative QCD, *Phys. Rev. Lett.* **102**, 162001 (2009); **111**, 199905(E) (2013).